

1 **Fully Coupled, High-Resolution Atmosphere-Ocean-Wave**
2 **Simulations of the Offshore Wind Energy Environment During**
3 **Hurricane Henri (2021)-of Hurricane Henri (2021): Implications for**
4 **Offshore Load Assessments**

5 Chunyong Jung¹, Pengfei Xue^{1,2,3}, Chenfu Huang^{2,3}, William Pringle¹, Mrinal Biswas⁴, Geeta Nain^{1,2},
6 and Jiali Wang¹

7 ¹Environmental Science Division, Argonne National Laboratory, Lemont, IL 60439, USA

8 ²Department of Civil and Environmental Engineering, Michigan Technological University, Houghton, MI 49931, USA

9 ³Great Lakes Research Center, Michigan Technological University, Houghton, MI 49931, USA

10 ⁴National Center for Atmospheric Research, Boulder, CO 80310, USA

11 *Correspondence to:* Chunyong Jung (cjung2@anl.gov); Pengfei Xue (pexue@mtu.edu)

12
13 **Abstract.** A new fully coupled modeling system, integrating atmosphere, ocean, and wave models, is presented to simulate
14 intricate interactions during tropical cyclones and explore their potential implications for offshore infrastructure. The system
15 is evaluated on Hurricane Henri (2021), chosen for its distinctive track along the U.S. northeast coast, an area of densely
16 populated regions and offshore wind energy zones. Three simulation setups are compared: atmosphere-only, atmosphere–
17 ocean, and a fully coupled atmosphere–ocean–wave model. Among them, the fully coupled model produces the most realistic
18 results, improving not only the storm intensity near the surface but also the wind structure from the near surface to the upper
19 atmosphere. Waves enhance ocean surface cooling with an additional 0.5 K reduction via ~~non-breaking~~ wave-induced vertical
20 mixing and modify wind interactions through wave-driven surface roughness. This more realistic representation of coupled
21 heat and energy exchanges between the atmosphere and ocean yield improved wind field patterns, which are critical for
22 comprehensive risk assessment pertaining to offshore ~~energy wind turbines~~ infrastructures. Furthermore, the coupled system
23 reasonably captures wind-wave misalignment during the storm, with the greatest misalignment in the left-front and rear-left
24 quadrants, while alignment occurs on the right side of the storm due to storm motion enhancing wave growth. These spatial
25 variations highlight the need to accurately model atmosphere–ocean–wave interactions for reliable wind load assessments.
26

27 **1 Introduction**

28 Tropical cyclones (TCs) are among the costliest and deadliest natural hazards in the U.S., responsible for \$945.9 billion in
29 damages and 6,502 fatalities from 1980 to 2019 (Smith, 2020). Although track forecasts have improved over recent decades,
30 the ability to predict TC intensity remains limited (DeMaria et al., 2014; Rappaport et al., 2009; Yamaguchi et al., 2017; Zao
31 et al., 2022). A key limitation lies in the incomplete representation of atmosphere-ocean interactions in models, particularly
32 storm-induced sea surface temperature (SST) cooling (e.g., DeMaria et al., 2007; Zhao et al., 2017, 2022). This cooling is
33 primarily driven by vertical mixing processes caused by strong TC-generated waves, intense upper-ocean shear, and
34 upwelling associated with divergent ocean currents (Emanuel, 1986; Schade and Emanuel, 1999; Wu et al., 2016). While
35 these air-sea interactions are recognized as critical drivers of storm intensity in a meteorological context, their implications
36 for the offshore built environment remain insufficiently explored.

37
38 ~~Current risk assessments conducted under hurricane conditions often simplify or omit these coupled feedback~~
39 ~~studies have explored TC dynamics using fully coupled atmosphere-ocean-wave models (e.g., Chen et al., 2007; Fan et al.,~~
40 ~~2009; Zhao et al., 2017, 2022), few have extended these frameworks to the domain of offshore wind energy risk assessment.~~
41 ~~Despite the significant impact of air-sea interactions on surface fluxes and hurricane wind structure, they are often overlooked~~
42 ~~in applied wind energy assessments and design studies conducted under hurricane conditions (e.g., Arthur, 2021; Chen et al.,~~
43 ~~2024; Roldán et al., 2023; Sanchez Gomez et al., 2023), potentially leading to -a disconnect between state-of-the-art~~
44 ~~numerical modeling and the practical evaluation of offshore structural vulnerabilities. This simplification can result in~~
45 ~~inaccurate representations of wind loading and an underestimation of structural vulnerabilities.~~

46 One critical gap in current hurricane-focused offshore wind assessments is the impact of wind-wave misalignment on
47 structural loads and potential damage. Such misalignment can significantly increase side-to-side turbine deflections and lead
48 to underestimations of fatigue loads by as much as 50% in floating systems. For instance, a recent study by Shanahan and
49 Fitzgerald (2025) found that wind-wave misalignment in floating offshore wind turbines can exceed 30° during hurricanes
50 and reach up to ~58° along exposed western coastal zones of Ireland. Additionally, Ma and Sun (2023) used large-eddy
51 simulations to model the coupled wind-wave loading on fixed-bottom offshore turbines, finding that under extreme events,
52 such as hurricanes, aerodynamic loading increases: the mean bending moment at both tower and monopile rises by ~6%, the
53 standard deviation of shear force increases by up to ~45%, and the bending movement variability increases by ~27%. These
54 findings highlight the need for dynamic, coupled modeling approaches that can capture the evolving interactions among wind,
55 waves, and currents, especially under extreme events, such as hurricanes (e.g., Chen et al., 2013; Barr and Chen., 2025).

56 However, most current modeling frameworks used for wind energy risk assessment fall short in this regard. Uncoupled
57 atmospheric models typically calculate surface roughness solely based on wind speed (e.g., via Charnock formulations),
58 neglecting without explicitly representing wave-induced momentum fluxes (e.g., Sanchez Gomez et al., 2023), which can
59 bias near-surface wind fields, shear profiles, and wind veer under extreme forcing. Statistical-parametric models, while

60 efficient for probabilistic loss estimation, represent hurricane winds using idealized radial wind profiles—such as studies that
61 use the classic Holland model (Arthur, 2021), the two-parameter Holland formulation (Chen et al., 2024), or recent
62 asymmetric extensions (Roldán et al., 2023). By ~~neglecting not explicitly accounting for~~ the evolving feedback among wind,
63 waves, and ocean currents, these approaches can underpredict or overpredict extreme gusts and rapid directional shifts that
64 critically drive turbine loading.

65 To ~~move beyond these idealized and uncoupled approaches, address these limitations,~~ this study introduces a newly developed
66 atmosphere-ocean-wave coupled modeling system that integrates a regional atmospheric mesoscale model with ocean and
67 surface wave models, both of which operate a high-resolution unstructured mesh. This framework, while sharing similarities
68 with the Coupled Ocean Atmosphere Wave and Sediment Transport (COAWST; Warner et al., 2010), is distinguished by
69 several key enhancements. First, it supports regional mesh refinement, allowing ultra-high resolution ocean grids over
70 targeted areas such as offshore wind farms. This feature provides more localized and detailed oceanic information, improving
71 the system’s utility for site-specific assessment. Second, our framework explicitly includes the effects of non-breaking wave
72 processes in the coupling system. These processes, which require custom implementation (e.g., Xu et al., 2023), are not part
73 of the standard COAWST model but are essential for realistically representing atmosphere-ocean-wave interactions,
74 especially under extreme wind conditions such as those associated with TCs.

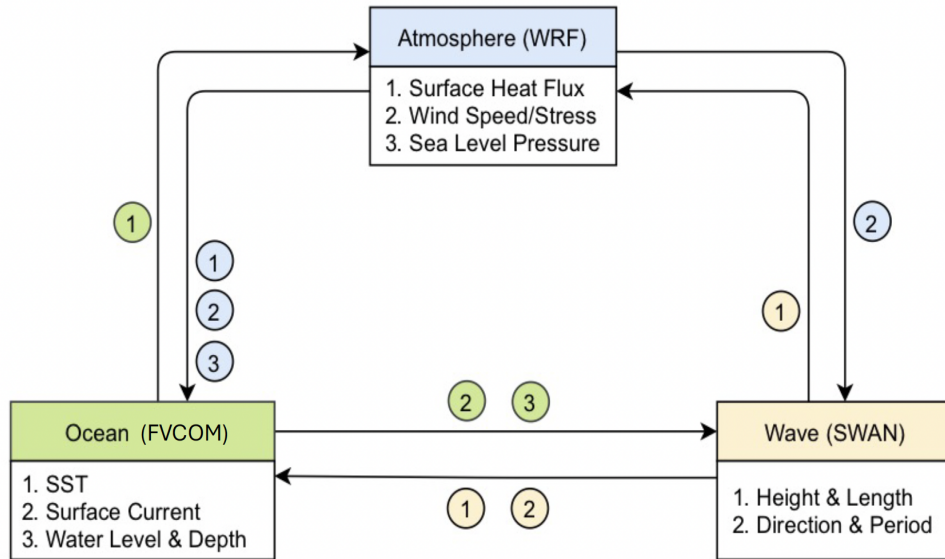
75 Within this modeling context, the present study focuses on characterizing the coupled offshore environmental forcing rather
76 than on turbine-level structural response. While turbine loads and wake recovery are not directly explored, the study examines
77 key aspects of atmosphere-ocean-wave interface that underpin such analyses. By assessing how coupling influences hub-
78 height wind speeds and vertical wind profiles, this work provides relevant meteorological and oceanographical information
79 that can inform future high-fidelity load modeling and offshore wind design studies and risk assessment. Accordingly, the
80 primary objective of this study is to demonstrate the capabilities of the newly developed coupled framework and to evaluate
81 its ability to resolve the complex atmosphere-ocean-wave processes that govern TC wind structure. We apply the system at
82 high resolution (3 km for both atmospheric and oceanic components near the U.S. Northeast Coast) to Hurricane Henri (2021)
83 as a case study.

84 ~~We apply this fully coupled system at high resolution (3km for both atmospheric and oceanic components near the U.S.~~
85 ~~Northeast Coast) to evaluate the impact of intercomponent coupling feedback on TC development, with a focus on the near-~~
86 ~~surface and lower boundary layer wind field. In this study, we selected Hurricane Henri (2021) to demonstrate the capabilities~~
87 ~~of the coupled system, providing insights into the role of wave dynamics in atmosphere-ocean modeling and their influence~~
88 ~~on storm wind structure, with a particular focus on processes at the air-sea interface and within the planetary boundary layer.~~

89 Henri was a Category 1 storm that made landfall in Rhode Island on 22 August 2021 ~~and traversed the~~. ~~Despite its weak~~
90 ~~intensity, Henri caused heavy rainfall, flooding, and power outages across the densely populated Northeast U.S., including~~
91 ~~New York and Boston. It also passed through the~~ offshore wind energy lease area on the northeast continental shelf. Extensive
92 observations, including airborne Doppler radar and dropsonde data near the eyewall, enable direct ~~comparison-evaluation of~~
93 ~~between~~ modeled against observations. This study represents a necessary step toward transitioning offshore wind energy

94 assessments from idealized or uncoupled parameterizations to a fully consistent, physics-based representation of
95 environmental forcing under extreme weather conditions. ~~and observed storm structures to assess model performance and~~
96 ~~atmosphere-ocean-wave coupling.~~

97 The development of the model, including detailed information on each model component and the coupler, is described in
98 Section 2. Section 3 describes the experimental design and data used for model validation using Hurricane Henri (2021) as a
99 working example. In Section 4 and 5, we present results and analysis, followed by the summary and discussions in Section
100 6.



101
102 **Figure 1. Schematic of coupled atmosphere-ocean-wave system and modelling used in this study.**

103 **2 Model Description**

104 The coupled atmosphere–ocean–wave modeling system integrates three core components: the Weather Research and
105 Forecasting (WRF) for atmospheric processes (V4.5.1; Skamarock et al., 2019), the Finite Volume Community Ocean Model
106 (FVCOM) for ocean circulation (V4.3.1; Chen et al., 2003, 2013), and the third-generation Simulating Waves Nearshore
107 (SWAN) for wave dynamics (Booij et al., 1999), with data exchanged via a coupler (Fig. 1). Hereafter, we refer to the coupled
108 WRF-FVCOM-SWAN model as C-WFS. These components run in parallel and interact through the OASIS3-MCT coupler
109 (Craig et al., 2017). Details on each model, recent improvements, and the coupling strategy are provided in Sections 2.1–2.2.

110 **2.1 Model Components**

111 WRF is a nonhydrostatic, quasi-compressible atmospheric model featuring boundary layer physics and various sub-grid scale
112 parameterizations to simulate meso- and macroscale motions. In this study, we modified the WRF code to incorporate the
113 wave slope-based sea surface roughness formulation from Taylor and Yelland (2001) into several surface schemes, including

114 MYNN (Nakanishi and Niino, 2009; Olson et al., 2019) and both the original and revised MM5 schemes (Dyer and Hicks,
115 1970; Jimenez et al., 2012; Paulson, 1970; Webb, 1970):

116

$$117 \quad Z_0 = 1200H_s \left(\frac{H_s}{L_p} \right)^{4.5} + \frac{0.11\nu}{u_*} \quad Z_0 \leq 0.00285 \quad (1)$$

118

119 where Z_0 is the surface roughness length, H_s is the significant wave height, L_p is the wavelength at the peak of spectrum, ν
120 is kinematic viscosity, and u_* is the friction velocity. Although C-WFS includes alternative wave-based formulations (e.g.,
121 Drennan et al., 2003; 2005), our tests showed that the capped Taylor and Yelland (2001) method yielded the optimal
122 performance for our case study.

123 The ocean component, FVCOM (V4.3.1), is a 3D, free-surface, prognostic coastal circulation model that solves the primitive
124 equations on an unstructured triangular grid using the finite-volume method. It enables dynamic interaction between ocean
125 and atmospheric conditions throughout the simulation. In this study, we modified FVCOM to include vertical mixing induced
126 by non-breaking waves, by adding a wave-related term to the turbulence eddy diffusivity B_v , following Ghantous and
127 Babanin (2014a,b) and Aijaz et al. (2017):

128

$$129 \quad B_v = \alpha A^3 \kappa \sigma e^{3\kappa z} \quad (2)$$

130

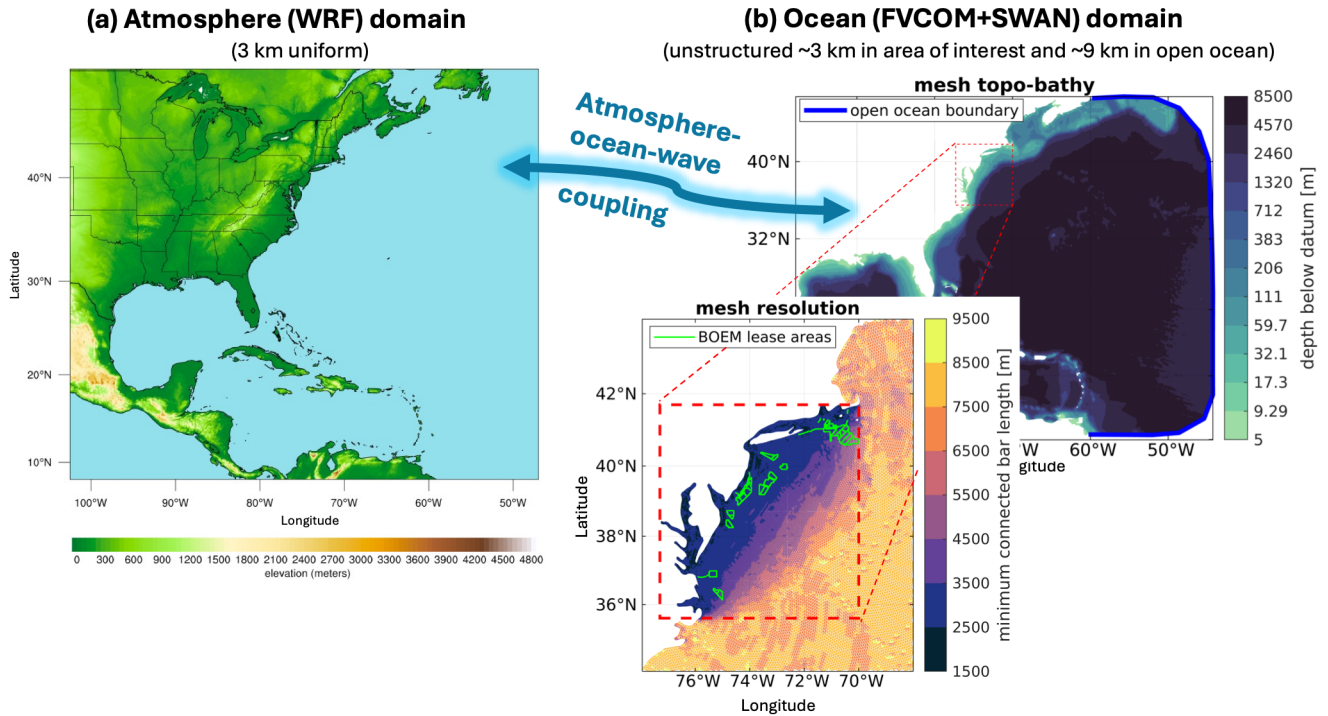
131 where $\alpha = 0.1$, A = wave amplitude ($H_s/2$), κ = wave number ($2\pi/L$), σ = peak wave frequency ($1/T_p$), z is water depth.

132 The wave model component, SWAN v41.01, is a third-generation spectral wave model developed at Delft University of
133 Technology that computes random, short-crested wind-generated waves in coastal regions and inland waters
134 (<http://swanmodel.sourceforge.net/>). It solves the evolution equation of wave action density in space time, frequency and
135 wave direction dimensions (Pringle and Kotamarthi, 2021). Various wave energy sources and sinks are modelled, including
136 wave generation by wind, wave decay due to whitecapping, bottom friction, depth-induced wave breaking, and energy
137 redistribution through nonlinear wind-wave interactions.

138 **2.2 Coupler and Coupling**

139 OASIS3-MCT is a parallel coupler that synchronizes 2-D and 3-D field exchanges. Figure 1 outlines the C-WFS coupling
140 framework and exchanged variables. WRF provides FVCOM with surface forcing—including friction velocity, winds, sea
141 level pressure, heat fluxes, and radiation fluxes—while receiving SST from FVCOM as over-ocean boundary conditions.
142 WRF also supplies wind fields to SWAN for wave simulations. In return, SWAN sends significant wave height and peak
143 wavelength to WRF, which uses them to calculate sea surface roughness based on Equation 1. FVCOM uses wave fields
144 from SWAN to compute radiation stress gradients, Stokes velocities, wave-enhanced bottom stresses, and non-breaking
145 wave-induced mixing; breaking wave mixing is included via stress gradients. FVCOM also provides surface currents to

146 SWAN, enabling Doppler shift effects from currents on wave behavior. This integrated coupling improves wave prediction
147 accuracy by capturing wave-current interactions more realistically.



148
149 **Figure 2. (a) WRF model domain with terrain height elevation, and (b) FVCOM and SWAN domain with bathymetric depths and**
150 **a zoom-in to the refined mesh grid along the northern U.S. East Coast and BOEM offshore lease areas.**

151 3 Application of C-WFS Modelling System

152 3.1 Experimental Design and Configuration

153 To evaluate the integrated impact of ocean and wave processes on TC simulations, three experiments were performed.
154 Experiment ‘A’ (atmosphere only) uses WRF with a 6-hourly updated SST. ‘AO’ couples WRF with FVCOM, enabling
155 atmosphere-ocean interaction but no wave effects. ‘AOW’ fully couples WRF, FVCOM, and SWAN via OASIS3-MCT,
156 allowing hourly, multi-way atmosphere-ocean-wave exchanges.

157 WRF is configured with a 3 km horizontal resolution and 46 vertical levels (12 below 100 m), covering much of the North
158 Atlantic basin (Fig. 2a). It uses 6-hourly 0.25° NCEP (National Centers for Environmental Prediction) Global Forecast
159 System (GFS; NCEP, 2015) analysis data for atmospheric initial and boundary conditions, with SSTs prescribed from GFS
160 in ‘A’. The model employs WSM6 microphysics (Hong and Lim, 2006), RRTMG radiation (Iacono et al., 2008), Yonsei
161 University PBL (Hong et al., 2006), and the Eta similarity surface layer scheme (Jimenez et al., 2012). No cumulus

162 parameterization is used, as 4 km resolution or less supports convection-permitting simulations (Akinsanola et al., 2024;
163 Kouadio et al., 2020; Qing and Wang, 2021; Sun et al., 2016).

164 The ocean domain (FVCOM) covers most of the WRF domain, with horizontal resolution ranging from ~ 9 km in the open
165 ocean to ~ 3 km over the continental shelf. It uses 40 sigma vertical layers to capture steep coastal bathymetry. Vertical mixing
166 processes are simulated using the Mellor–Yamada level-2.5 (MY25) turbulence closure model (Mellor and Yamada, 1982),
167 and horizontal diffusivity is computed using the Smagorinsky numerical formulation (Smagorinsky, 1963). Initial and
168 boundary conditions for currents, temperature, salinity, and water level are provided by $1/12^\circ$ HYCOM (Hybrid Coordinate
169 Ocean Model) analysis data (Cummins and Smedstad, 2014).

170 The wave model domain matches the FVCOM domain, using ~ 12 km horizontal resolution. The wave spectrum is divided
171 into 36 directional and 24 frequency bins (0.04–1 Hz). Wave physics include Komen et al. (1984) for growth and
172 whitecapping, Madsen et al. (1988) for bottom friction, and a constant depth-limiting breaker index, all with default settings.
173 Swell boundary conditions are omitted due to minimal impact at the eastern boundary, and the model is initialized from a
174 quiescent state.

175 All experiments were initialized at 18:00 UTC on 19 August, 2021, and simulated for 102 hours. Nudging techniques were
176 intentionally omitted to better isolate the effects of atmosphere–ocean–wave coupling on TC characteristics. Additional tests
177 using various physics schemes and forcing datasets (e.g., ERA5) confirmed the robustness and low sensitivity of the results
178 to model configuration choices, although the supporting results are not presented in this manuscript.

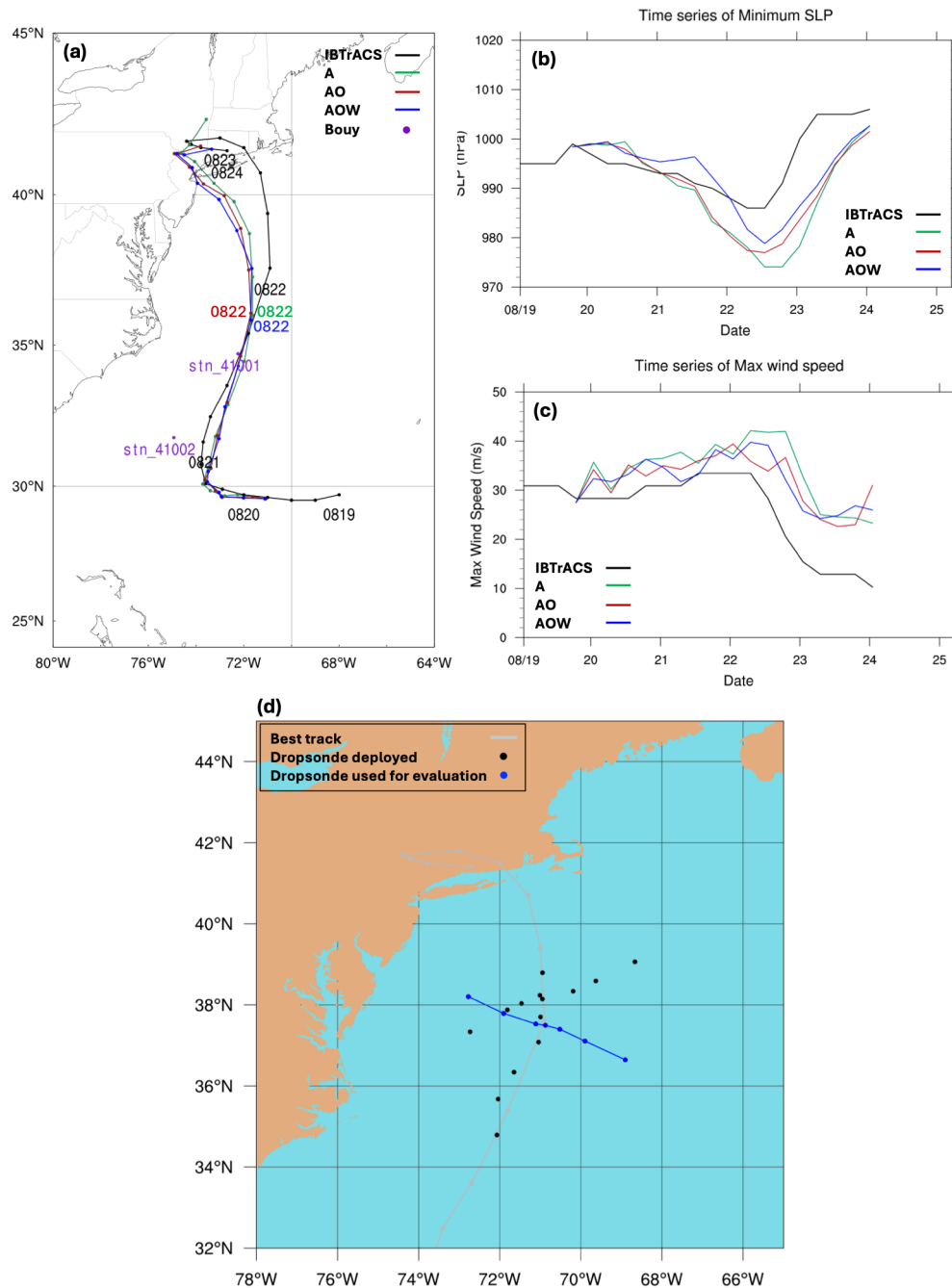
179 **3.2 Method and Data**

180 Model results are evaluated against several observational datasets, including International Best Track Archive for Climate
181 Stewardship (IBTrACS; Knapp et al., 2010), which provides TC position, minimum sea level pressure (SLP), and maximum
182 10-m sustained winds at ~ 6 -hour intervals, and airborne observations. The airborne data include the Tropical Cyclone Radar
183 Archive of Doppler Analyses with Recentering (TC-RADAR; Fischer et al., 2022) and dropsondes from NOAA’s Hurricane
184 Research Division. TC-RADAR contains X-band Doppler radar data from NOAA’s WP-3D aircraft, scanning in front and
185 back directions to produce detailed 3-D analyses of TC inner-core structure. Each mission typically includes 3–4 center passes,
186 with storm-centered “recentering” techniques used to generate gridded analyses. Our simulations adopt the same storm-
187 centered coordinates for direct comparison. A $300 \text{ km} \times 300 \text{ km}$ grid is centered on the grid cell with minimum SLP in each
188 dataset. To fill the 0–0.5 km altitude gap not captured by radar, we include dropsonde data. Due to slight differences in storm
189 track and speed between the model and observations (Fig. 3), dropsonde positions are adjusted relative to the storm center
190 (e.g., Creasey and Elsberry, 2017). Seven dropsondes (shown in Fig. 3d) from a single flight across the storm center were
191 selected for evaluation; this flight crossed the storm from east to west within 50 minutes from 23:21 UTC on 21 to 00:11
192 UTC on 22 August 2020 (with exact times indicated in Fig 3d), 12 hours before peak intensity.

193 Modeled ocean surface waves are compared with observations from two National Data Buoy Center (NDBC, 2008) buoys,
194 41001 and 41002, located on the left of the storm track on the continental slope. While there are more buoy locations, our

195 focus is on the variation of storm-induced winds and waves along Henri's track. We exclude stations near the U.S Northeast
196 Coast due to the models' track bias after 22 August (more discussion in Section 4). The buoy data provides surface wind and
197 wave information, including surface wind speed, significant wave height, and peak wave period and direction. In addition to
198 in-situ NDBC buoy measurements, we compiled a series of daily SST data from the Operational Sea Surface Temperature
199 and Ice Analysis (OSTIA; Good et al., 2020) at $0.05^\circ \times 0.05^\circ$ resolution to determine the pre- and post-storm environment
200 as well as the difference between them.

201 The radius of maximum wind (RMW) defines the location of the maximum winds in a TC and is critical to understanding
202 intensity change as well as hazard impacts. In this study, we azimuthally average the vertical profiles of the seven dropsondes
203 and the simulations of wind speed relative to RMW to define the areas within and beyond the eyewall, allowing for a detailed
204 comparison of the storm's inner- and outer-core regions. _____



206

207 **Figure 3. Comparison of simulated (a) track, (b) minimum sea-level pressure (SLP), and (c) maximum 10-m wind speed of**
 208 **Hurricane Henri with IBTrACS Best Track data from 18 UTC 19 to 00 UTC 24 August 2021. Black lines show IBTrACS data;**
 209 **green, red, and blue lines represent experiments 'A,' 'AO,' and 'AOW,' respectively. Panel (d) shows the IBTrACS track (grey)**

210 with dropsonde positions (black and blue dots). The seven dropsondes shown as blue dots were released during a single NOAA
211 WP-3D flight that traversed the storm center from west to east over approximately 50 minutes (23:21 UTC 21 to 00:11 UTC 22
212 August). These dropsondes were used to evaluate model performance. Purple dots in (a) denote buoy stations 41001 and 41002
213 from the National Data Buoy Center.

215 4 Model Validation

216 4.1 Track and Intensity

217 Figure 3 presents the tracks, SLP minima, and surface wind speed maxima derived from the three simulations alongside
218 IBTrACS. We emphasize at the outset that the purpose of this evaluation is not to assess forecast skill, but to provide a
219 baseline comparison that enables interpretation of how atmosphere-ocean-wave coupling alters storm evolution and wind
220 structure relative to partially coupled or uncoupled configurations.

221 The results indicate that variations in Henri's tracks across the three experiments show only minor differences are minimal
222 (Fig. 3), consistent with previous findings suggesting that TC tracks are predominantly controlled by large-scale atmospheric
223 circulation processes, rather than by atmosphere-ocean interactions at the temporal and spatial scales resolved in these models
224 (e.g., Zambon et al., 2014). The root-mean square error (RMSE, Table 1) of position indicates all three simulations have
225 similar track errors, with values of 123.7 km for 'A', 119.4 km for 'AO', and 126.1 km for 'AOW.' Higher errors stem mainly
226 from deviations after 00 UTC on 22 August, likely due to biases in midlatitude upper-level wave patterns (e.g., troughs and
227 ridges) affecting the storm embedded in the baroclinic zone. While Ppreliminary sensitivity tests indicate that show spectral
228 nudging can reduce track errors, nudging is intentionally excluded here to avoid constraining storm evolution and to better
229 isolate the physical effects of. ~~However, as the study focuses on atmosphere-ocean-wave interactions, in Hurricane Henri's~~
230 ~~evolution, all simulations are conducted without nudging, and All~~ subsequent analyses therefore reflect ~~those~~ unconstrained
231 results.

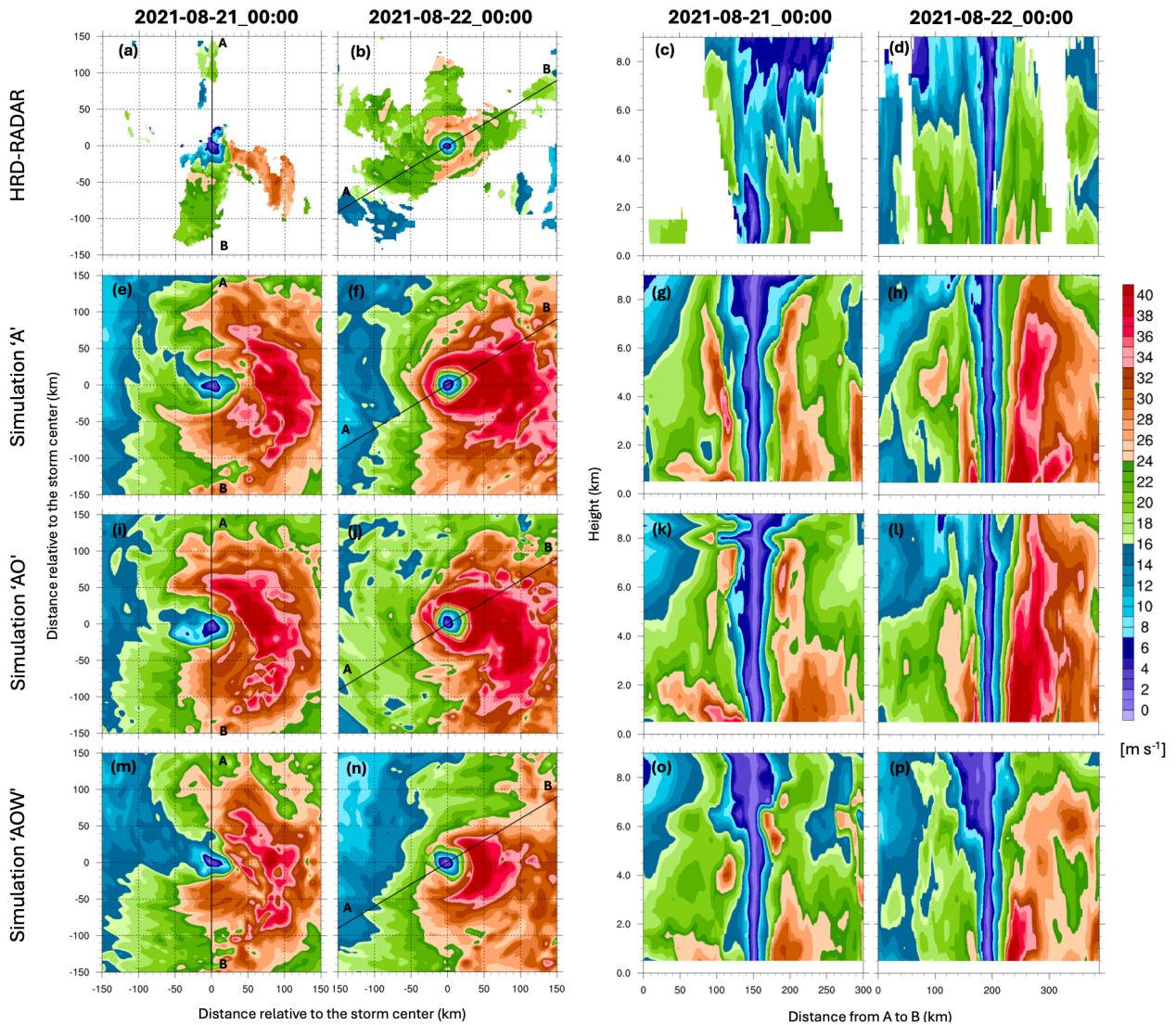
232 In contrast to track, all three experiments overestimate storm intensity in terms of Mminimum SLP throughout most of Henri's
233 lifecycleshows noticeable differences between the modeled storms 12 hours after the simulation starts (Fig. 3b). ~~While all~~
234 ~~three simulated storms show an overestimation throughout nearly the entire lifecycle of the storm, especially when they reach~~
235 ~~their~~ particularly near peak at 12 UTC on 22 August, Nevertheless, systematic differences emerge among the experiments.
236 Both ocean-coupled simulations ('AO' and 'AOW') reduce the magnitude of SLP overestimation relative to 'A.' ~~the~~
237 ~~magnitude of this overestimation is reduced in 'AO' and 'AOW' compared to 'A.'~~ In 'AOW', the overestimation of minimum
238 SLP is delayed until 00 UTC on 22 August, after which it reaches the weakest peak minimum SLP among the three. This
239 results in the lowest RMSE in minimum SLP (Table 1). These temporal trends also apply to the maximum surface wind speed
240 (Fig. 3c and Table 1), demonstrating a reduction in overestimation of maximum surface wind speed in both 'AO' and 'AOW'
241 compared to 'A.' Between the experiments 'AO' and 'AOW,' while 'AOW' generally exhibits weaker wind speeds compared
242 to 'AO,' it becomes stronger as the storm approaches and reaches its peak intensity, in contrast to the findings for minimum

243 SLP. This apparent decoupling between these two intensity metrics highlight the role of wave-modulated surface roughness
244 and air-sea momentum exchange, and it motivates the mechanistic analysis presented in The potential physical processes
245 underlying this discrepancy are discussed in Section 54.3.
246 Overall, while the simulations exhibit clear deficiencies in. rack and intensity, the consistent and systematic differences
247 among ‘A’, ‘AO’, and ‘AOW’ provide a useful framework for diagnosing how coupled ocean and wave processes influence
248 storm structure. These relative differences—rather than absolute forecast accuracy—form the basis for the process-oriented
249 analysis that follows.

250
251 **Table 1. Root mean square error (RMSE) for each simulation in terms of minimum sea level pressure (hPa), maximum surface**
252 **wind speed (m s^{-1}), and cyclone track (km).**

Experiment	Min. sea level pressure (hPa)	Max. surface wind speed (m/s)	Cyclone track (km)
A	9.4	10.2	123.7
AO	7.9	8.7	119.4
AOW	6.4	8.3	126.1

253
254



255

256 **Figure 4.** NOAA WP-3D airborne Doppler radar (TC-RADAR) wind speeds at the 1-km level are shown in the top row, with model-
 257 simulated wind speeds from the ‘A’ (second row), ‘AO’ (third row), and ‘AOW’ (fourth row) simulations of Hurricane Henri (2021)
 258 at 00 UTC on 21 (first and third columns) and 22 August (second and fourth columns). Vertical cross-sections along the A–B line
 259 (marked in the left two panels) are shown in the right two columns. All horizontal fields are plotted in a 300×300 km storm-
 260 centered domain.

261 4.2 Storm Wind Structure

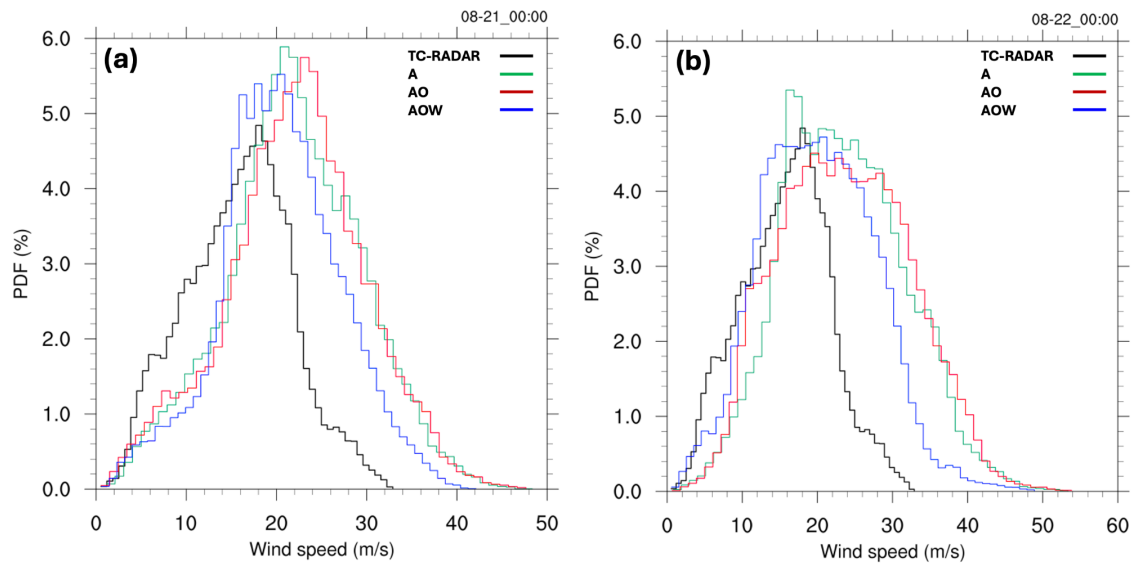
262 Figures 4a–d show 1-km level wind speeds and vertical profiles from TC-RADAR at 00 UTC on 21 and 22 August 2021,
 263 along the black lines in Figs. 4a–b. On 21 August, observations reveal a strongly asymmetric wind field, with the highest
 264 winds concentrated on the storm's right side. This asymmetry results from the combination of Henri's cyclonic circulation
 265 and its poleward motion, which enhances wind speeds on the right through additive forward momentum. The vertical cross-

266 section (Fig. 4c) along line A–B shows wind speeds $>20 \text{ m s}^{-1}$ largely confined below 4 km on the southern side but extending
267 to 8 km on the northern side. By 00 UTC on 22 August, 12 hours before its minimum central pressure, Henri’s wind field
268 becomes more symmetric and compact, with a closed eyewall and winds exceeding 24 m s^{-1} (Figs. 4b,d). A clear calm zone
269 is evident within the eyewall, extending up to 9 km. Strong winds are more evenly distributed around the center, but remain
270 strongest on the right. Corresponding model-simulated wind profiles and 1-km level horizontal wind fields at both times are
271 shown in Figs. 4e–p.

272 All three simulated storms reasonably capture Henri’s structural evolution—from a broad, asymmetric wind pattern with
273 strong right-side winds at 00 UTC 21 August (as seen in TC-RADAR) to a more compact, symmetric structure by 00 UTC
274 22 August. However, the simulations, especially experiments ‘A’ and ‘AO,’ overestimate wind intensity both horizontally
275 and vertically. The fully coupled run ‘AOW’ reduces this bias, producing more realistic radial wind profiles at 1 km along
276 line A–B (Fig. S1) and achieving the highest Pearson correlations with TC-RADAR ($r = 0.95$ for horizontal distribution and
277 0.72 for vertical cross-section). To assess wind distribution more comprehensively, we use probability density functions
278 (PDFs) across all available TC-RADAR grid cells ($0.5\text{--}9 \text{ km}$ altitude within a $300 \times 300 \text{ km}$ domain centered on the storm).
279 All simulations skew toward higher wind intensities, but ‘AOW’ shows improved performance, especially in the upper tail,
280 suggesting reduced wind bias during storm intensification (Fig. 5).

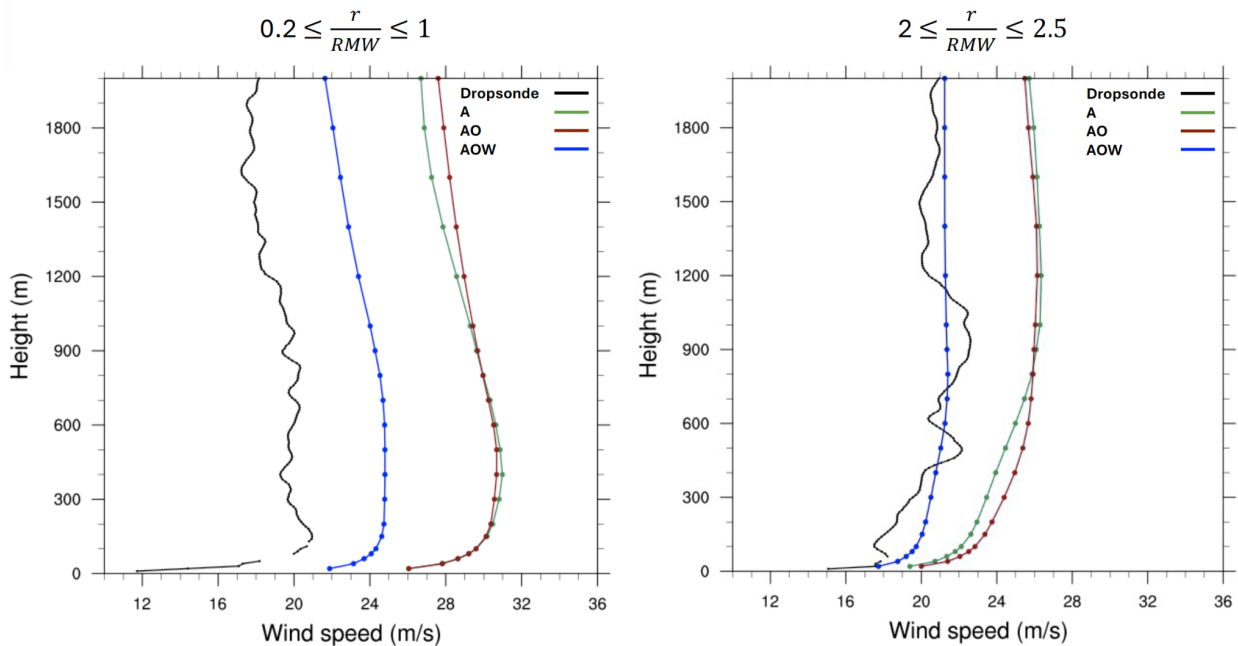
281 While TC-RADAR provides rich horizontal and vertical coverage, it only samples above 0.5-km, limiting surface-level
282 validation. Dropsonde data help bridge this gap. Figure S2 shows vertical cross-sections up to an altitude of 3.2 km along the
283 blue line in Fig. 3d: consistent with TC-RADAR, strongest winds appear 10–30 km east of the center, while much weaker
284 winds dominate the western side. These asymmetries are captured in all simulations, though generally overestimated.

285 Azimuthally averaged vertical profiles (Fig. 6) in the inner-eyewall ($0.2 \leq r/\text{RMW} \leq 1$) and outer-eyewall ($2 \leq r/\text{RMW} \leq 2.5$)
286 regions at the dropsonde locations further confirm that all simulations overestimate low-level winds (below 2 km). However,
287 ‘AOW’ aligns more closely with observations, particularly in the outer-eyewall. This improvement is critical, as it provides the
288 necessary baseline environmental forcing for offshore wind energy studies, including high-fidelity load modeling and risk
289 assessment, where accurate wind profiles near hub height are essential for turbine design, placement, and risk mitigation in
290 storm-prone regions.



291

292 **Figure 5: Probability density function of wind speed in a 300 km x 300 km storm-centered coordinate, considering vertical levels**
 293 **from 0.5 km to 9 km above the ground, for 00 UTC on 21 (a) and 22 August (b) 2021. The data are derived from TC-RADAR**
 294 **(black lines), experiment 'A' (green lines), experiment 'AO' (red lines), and experiment 'AOW' (blue lines).**



295 **Figure 6. Vertical profiles of azimuthally averaged wind speed for dropsondes (black lines), experiment 'A' (green lines),**
 296 **experiment 'AO' (red lines), and experiment 'AOW' (blue lines). The vertical profiles are azimuthally averaged in the inner-eyewall**
 297 **region (left; $0.2 \leq r/RMW \leq 1$) and the outer-eyewall regions (right; $2 \leq r/RMW \leq 2.5$), based on the locations of the seven dropsondes**
 298 **highlighted in blue dots in Fig. 3d at 00 UTC on 22 August 2021. RMW indicates radius of maximum wind, and r shows radius**
 299 **relative to the storm center.**
 300

301 4.3 Sea Surface Temperature

302 From the ocean's perspective, SST and surface roughness are key factors influencing TC intensity, as they directly affect the
303 exchange of heat, moisture, and momentum between the ocean and the storm (Zambon et al., 2014, 2021; Zhao et al., 2022).
304 The main distinction among the three simulations lies in how SST and ocean surface roughness are represented, influencing
305 surface enthalpy and momentum fluxes through air-sea interactions. Accordingly, SST is used both as an indicator of storm
306 evolution and as a dynamic driver of intensity across the three simulations. Therefore, evaluating how well the coupled model
307 reproduces observed SST is critical for assessing its ability to realistically capture ocean dynamics and storm-ocean
308 interactions.

309 Figure 7 shows the SST distribution across the simulation domain for all three experiments, along with OSTIA observations
310 from 12 UTC on 20 to 12 UTC on 23 August 2020. Since OSTIA provides daily SST data, the statistics in Table 2 represents
311 an average over these four days. In experiment 'A', the SST is derived from GFS, and is technically driven by observed SST
312 data. Therefore, it captures key large-scale features well, such as the Gulf Stream and warm waters along the Gulf Coast.
313 However, it consistently underestimates SST across the domain during this period. In addition, its relatively low resolution
314 (0.25°) limits its ability to capture small-scale SST patterns, contributing to the higher RMSE values shown in Table 2.

315 The ocean-coupled simulations ('AO' and 'AOW'), which are driven by oceanic initial and boundary conditions from the
316 HYCOM analysis, successfully capture major SST features such as the Gulf Stream and Gulf Coast, with enhanced spatial
317 detail. This improved representation contributes to lower RMSE values compared to the atmosphere-only simulation ('A')
318 (Table 2). However, both 'AO' and 'AOW' tend to overestimate SSTs in the open North Atlantic and underestimate them near
319 the northeastern U.S. coast (Figs. 7d, l, p), likely due to cold wakes generated by the simulated storms and deviations in their
320 tracks from observations. Nevertheless, the ocean-coupled simulations reasonably reproduce the observed SST, with RMSE
321 values of 0.564 and 0.577 for 'AO' and 'AOW', respectively—lower than that of 'A'—while maintaining comparable pattern
322 correlation overall (Table 2).

323 To assess the potential influence of track biases on SST and MSLP, we first examined 'A' simulation. It exhibits
324 overintensification of MSLP, a consequence of its simulated track failing to coincide with the observed cold wakes in the
325 GFS data. This misalignment prevents the realistic capture of crucial atmosphere-ocean heat and moisture exchanges.
326 Conversely, ocean-coupled simulations ('AO' and 'AOW') more accurately represent storm-induced modifications to surface
327 energy and momentum fluxes. By explicitly modeling SST cooling along their simulated storm paths, these coupled runs
328 achieve a more realistic depiction of storm intensity. In particular, 'AOW' simulation shows enhanced SST cooling around
329 the time of peak intensity and thereafter, further contributing to a reduction in MSLP. Spatial and temporal averaging of SST
330 within a $300 \text{ km} \times 300 \text{ km}$ storm-centered domain from 12 UTC on 21 August to 12 UTC on 22 August indicates an SST of
331 299.7 K for 'AOW', compared to 300.2 K previously—representing a 0.5 K reduction and bringing it closer to the OSTIA
332 value of 299.1 K (Table 3). Details of the storm-centered SST distributions are provided in the Supplementary Information
333 ([Fig. S3](#)). This improved performance in 'AOW' can be attributed to the effect of wave-induced vertical mixing, which

334 effectively brings cooler subsurface water to the surface, aligning with our previous discussion and prior research (e.g., Wada
335 et al., 2010; Zambon et al., 2014)

336

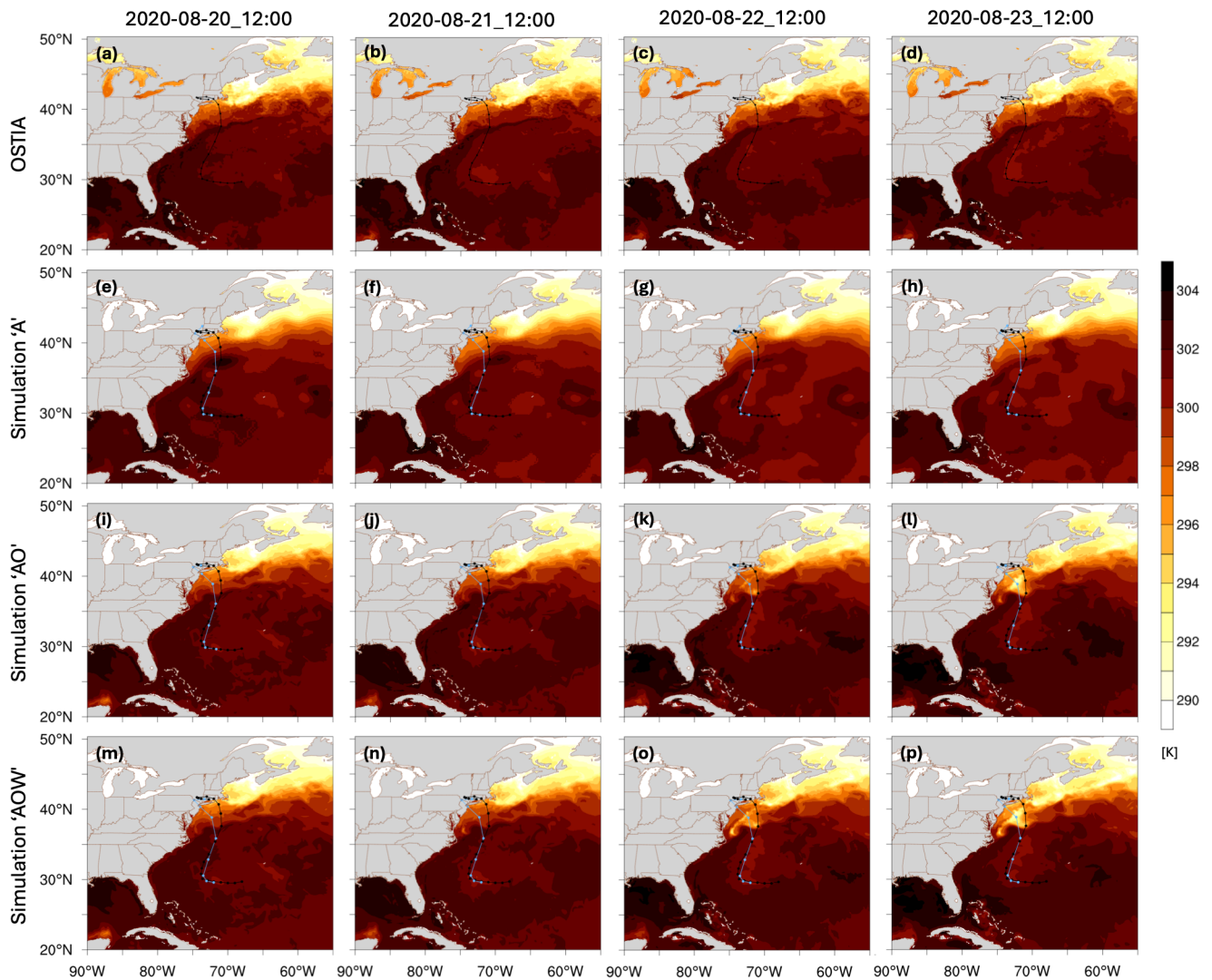
337 **Table 2. Temporally averaged root mean square error (RMSE) and Pearson product- moment coefficient of linear correlation (r)**
338 **for SST in each simulation compared to OSTIA SST observations from 12 UTC on 20 to 12 UTC 23 August, 2021.**

Experiment	RMSE	Pattern Correlation
A	0.631	0.992
AO	0.564	0.991
AOW	0.577	0.990

339

340 **Table 3. Spatially averaged SST (K) derived from A, AO, AOW, and OSTIA observation in a 300 km x 300 km storm-centered**
341 **coordinate at 12 UTC 20, 12 UTC 21, and 12 UTC 22 August.**

Experiment	12 UTC 20 August	12 UTC 21 August	12 UTC 22 August
A	302.01	301.81	299.37
AO	301.79	301.83	298.47
AOW	301.76	301.70	297.70
OSTIA	302.15	301.43	296.76



342

343 **Figure 7. Vertical-SST distribution (K) for OSTIA (top panelrow), 'A' (second rowpanel), 'AO' (third panelrow) and 'AOW'**
 344 **(bottom rowpanel) at 12 UTC on 20 (first column), 21 (second column), 22 (third column), and 24 August 2020 (fourth column).**
 345 **The black dots and lines indicate the best track derived from IBTrACS. The light blue dots and lines depict simulated storm**
 346 **locations and tracks.**

347

4.4 Ocean Surface Waves

348

This section assesses how accurately our model simulates ocean surface waves during Hurricane Henri at two NDBC buoy
 349 locations. During Henri's primary development, buoy 41001 was directly in the path of the eyewall, while buoy 41002 was
 350 positioned approximately 120 km to the left of the storm's center during its earlier stages (Fig. 38a). The fully coupled
 351 experiment successfully captures the general temporal trends in wind speed at both sites (Figs. 8ba–eb). However, a slower
 352 simulated storm translation speed, particularly between 06:00 and 12:00 UTC on 21 August, led to a delay of roughly 12

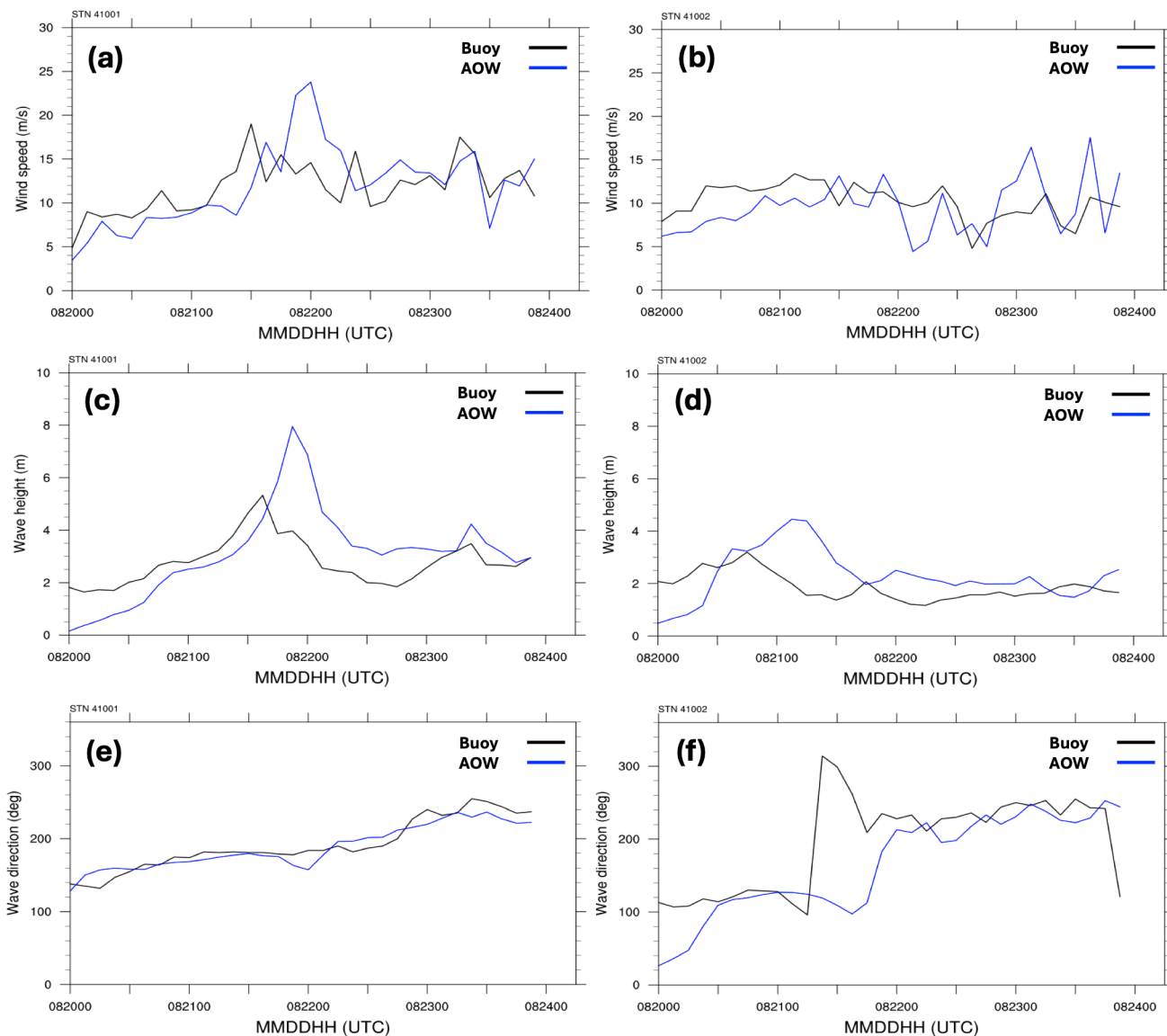
353 hours in both wind speed and wave height peaks. Furthermore, the model overestimates significant wave height by about 1–
354 2.5 m at both locations during peak conditions (Figs. 8dc–ed). At station 41001, this overestimation is primarily attributable
355 to discrepancies in wind speed. For station 41002, an additional contributing factor is the model's faster simulated translation
356 speed—6.3 m s⁻¹ compared to the observed 4.8 m s⁻¹ between 00:00 and 06:00 UTC on 21 August. It is well-established that
357 increased forward motion enhances wind speed and wave growth on a storm's right side, leading to higher waves (Chen et
358 al., 2013). While the model accurately reproduces wave direction at station 41001, it fails to capture the sharp directional
359 shift observed at station 41002 between 06:00 and 09:00 UTC on 21 August (Figs. 8ef–gf). This discrepancy may stem from
360 the model's increased wave height and wavelength, which can suppress rapid directional changes. Despite these biases in
361 wave height magnitude and timing, the model generally provides a reasonable representation of wave behavior at both
362 locations and successfully captures key trends in storm-induced wave dynamics during Hurricane Henri.

363 Understanding the accuracy of modeled ocean surface waves, particularly their directional characteristics, is crucial because
364 previous investigations into TC wind impacts on offshore wind turbines (e.g., Sanchez Gomez et al., 2023; Wei et al., 2017;
365 Itiki et al., 2023) have often relied on atmosphere-only frameworks or empirical wave representations. As noted in several of
366 those studies such approaches necessarily simplify or exclude explicit wind-ocean-wave coupling processes, which may
367 influence both direct and indirect load pathways. These acknowledged modeling limitations motivate the need for coupled
368 approaches that better represent wind-wave interactions when assessing offshore wind risk extreme conditions. overlooked
369 the complexities of wind-ocean-wave interactions. This oversight, common in atmosphere-only or empirical models,
370 significantly limits accurate risk prediction for offshore infrastructure by failing to capture both direct and indirect impacts.
371 For instance, Ma and Sun (2023) demonstrated that under extreme wind-wave conditions, such as those in hurricanes,
372 coupling between wind and wave dynamics significantly increases the aerodynamic loads on offshore wind turbines. This
373 coupling markedly amplifies the variability of those loads, suggesting that traditional decoupled models may underestimate
374 the structural demands during such severe events.

375 Figure 9 shows that wind and wave alignment varies considerably over time, with periods of near co-alignment interspersed
376 with misalignments. The directional divergence is site-specific, highlighting the influence of localized impact depending on
377 locations relative to the storm center. 'AOW' captures key characteristics of directional interactions, reproducing the timing
378 and magnitude of misalignment trends reasonably well (Figs. 9 bottom panel). Notably, the simulations reflect-capture the
379 directional sensitivity at both sites, suggesting fidelity in representing storm-induced wave generation and propagation. By
380 resolving wind-wave misalignment, the fully coupled modeling system provides a more physically consistent description of
381 the environmental conditions relevant to offshore infrastructure under extreme events such as TCs.
382 implying that the fully coupled modeling system provides a more realistic representation of the complex environmental loads
383 on offshore wind turbines, particularly under extreme conditions like TCs.

384 Figure 10 illustrates simulated ocean surface wave conditions and 10-m wind vectors from 'AOW' experiment at 12:00 UTC
385 on 22 August. Consistent with prior studies (e.g., Chen et al., 2013; Wright et al., 2001), TC-induced wave fields typically
386 exhibit asymmetry, with the highest significant wave heights occurring in the front-right quadrant. This pattern is clearly

387 evident in our simulation, as Henri moves northwest, producing the largest waves in its right and front-right quadrants (Fig.
 388 10a). The storm's motion further enhances wave growth on the right side due to a longer fetch (Figs. 10a-b). Significantly,
 389 directional misalignment between wind and waves is apparent across most storm quadrants, except on the right side where
 390 both wind and waves are aligned, also consistent with previous findings (Fig. 10d). This widespread misalignment as well as
 391 aligned directions highlight the complex atmosphere-wave interactions that necessitate careful consideration in offshore wind
 392 load assessments.

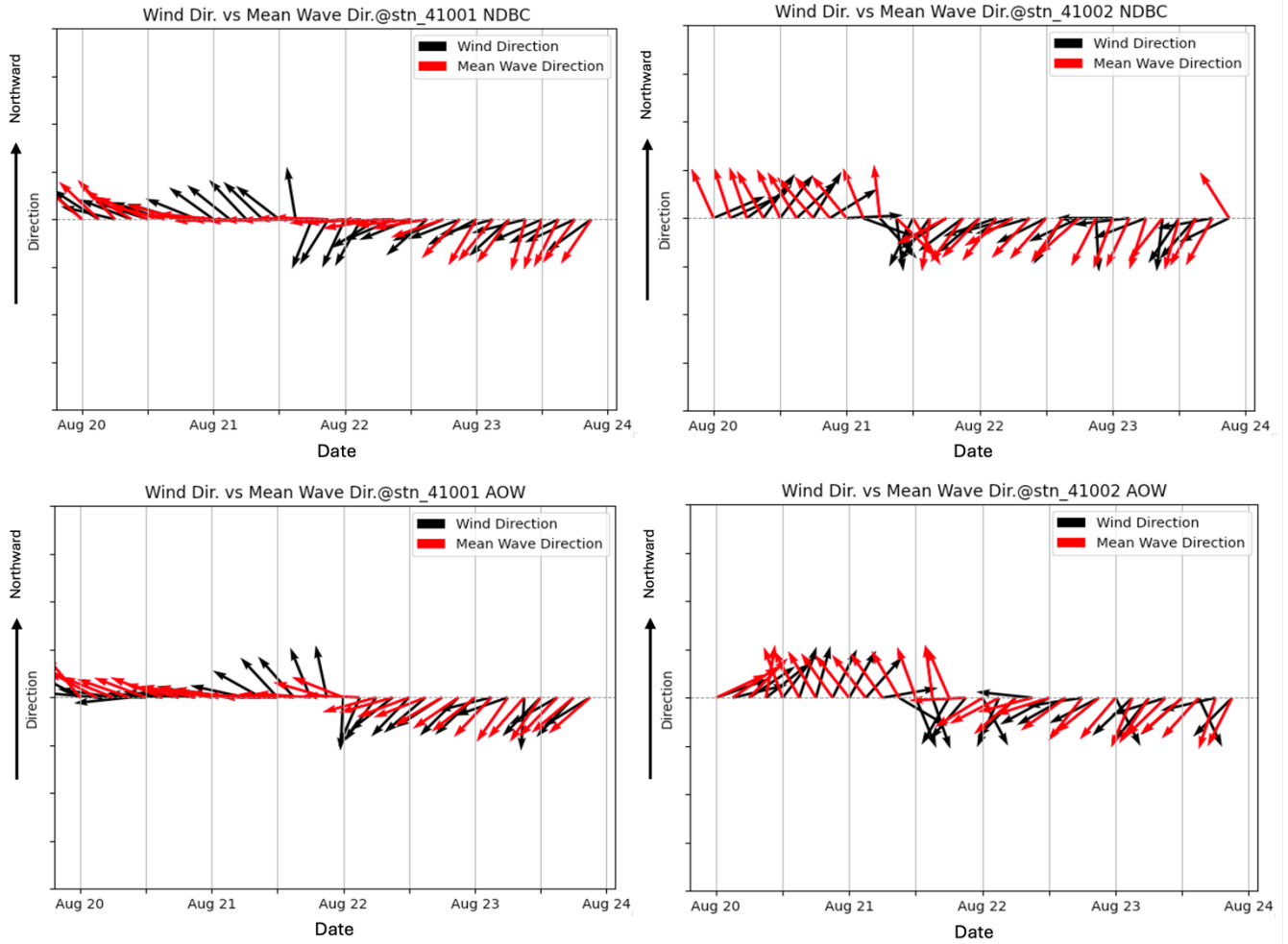


393

394 **Figure 8. Comparison of the 'AOW' simulation (blue) with observations (black) for Hurricane Henri from 00 UTC 20 to 00 UTC**
 395 **24 August 2021: (a) track, (b) wind speed (m/s), (c) significant wave height (m), and (e) wave direction. The right**

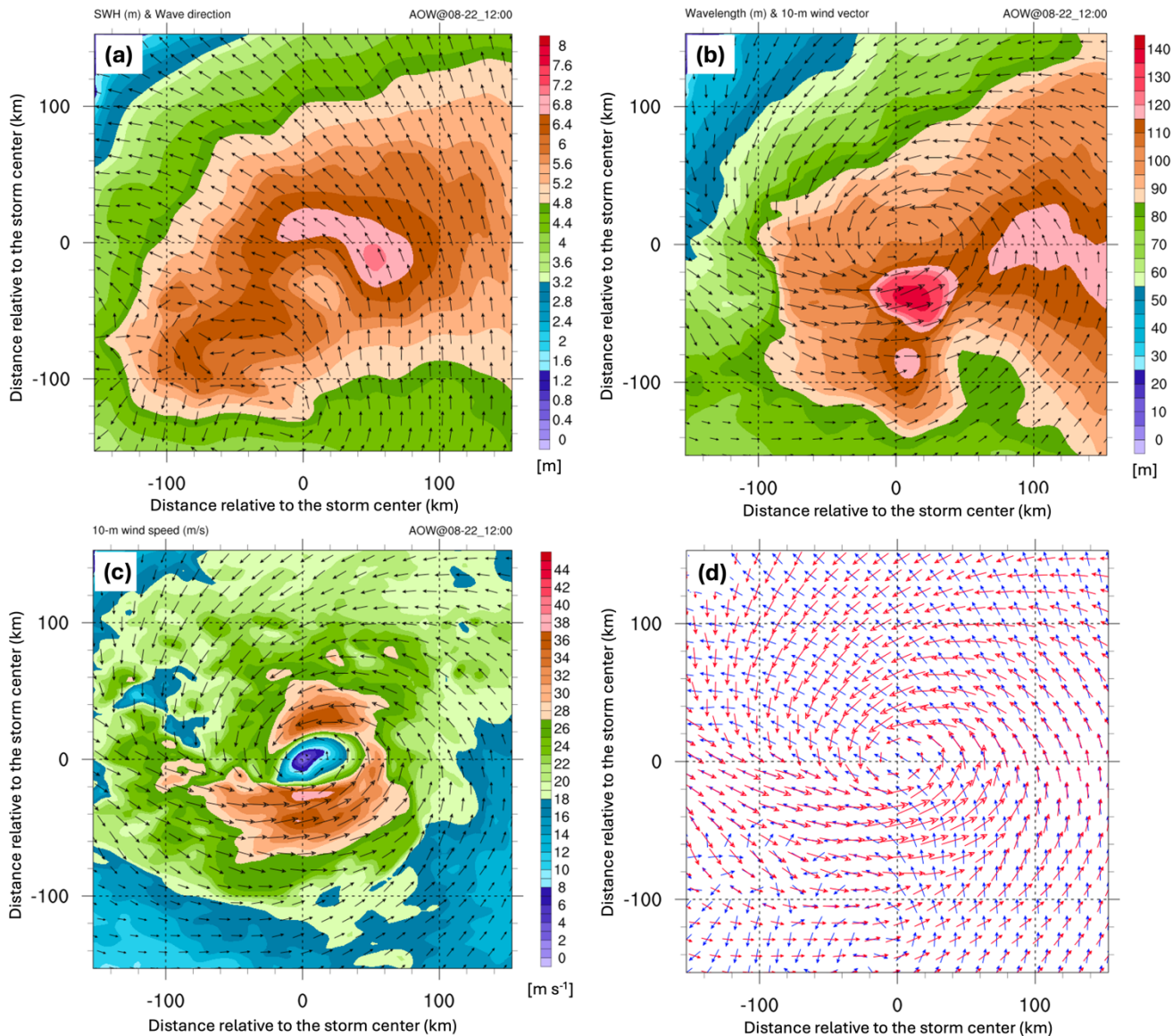
396
397

column shows data from station 41001, while the left column depicts station 41002. The locations of stations 41001 and 41002 are shown in Figure 3(a). Panels (b), (d), and (f) show data from station 41001, while (c), (e), and (g) show station 41002.



398
399
400
401

Figure 9. Time series comparison of surface wind direction and mean ocean surface wave direction at two NDBC buoy stations, 41001 (left column) and 41002 (right column), derived from NDBC buoys (top panel) and experiment 'AOW' (bottom panel).



402
 403 **Figure 10.** The fully coupled model output at 12 UTC on 22 August 2021 includes: (a) significant wave height (shaded; in meters)
 404 and wave direction, (b) mean wavelength (shaded; in meters) and 10-m wind, (c) 10-m wind speed (shaded; in m/s) and vectors,
 405 and (d) wave (blue) and wind (red) vectors. All plots are in a 300 × 300 km storm-centered domain, with a 20 m/s reference wind
 406 vector shown in panels (b) and (c).

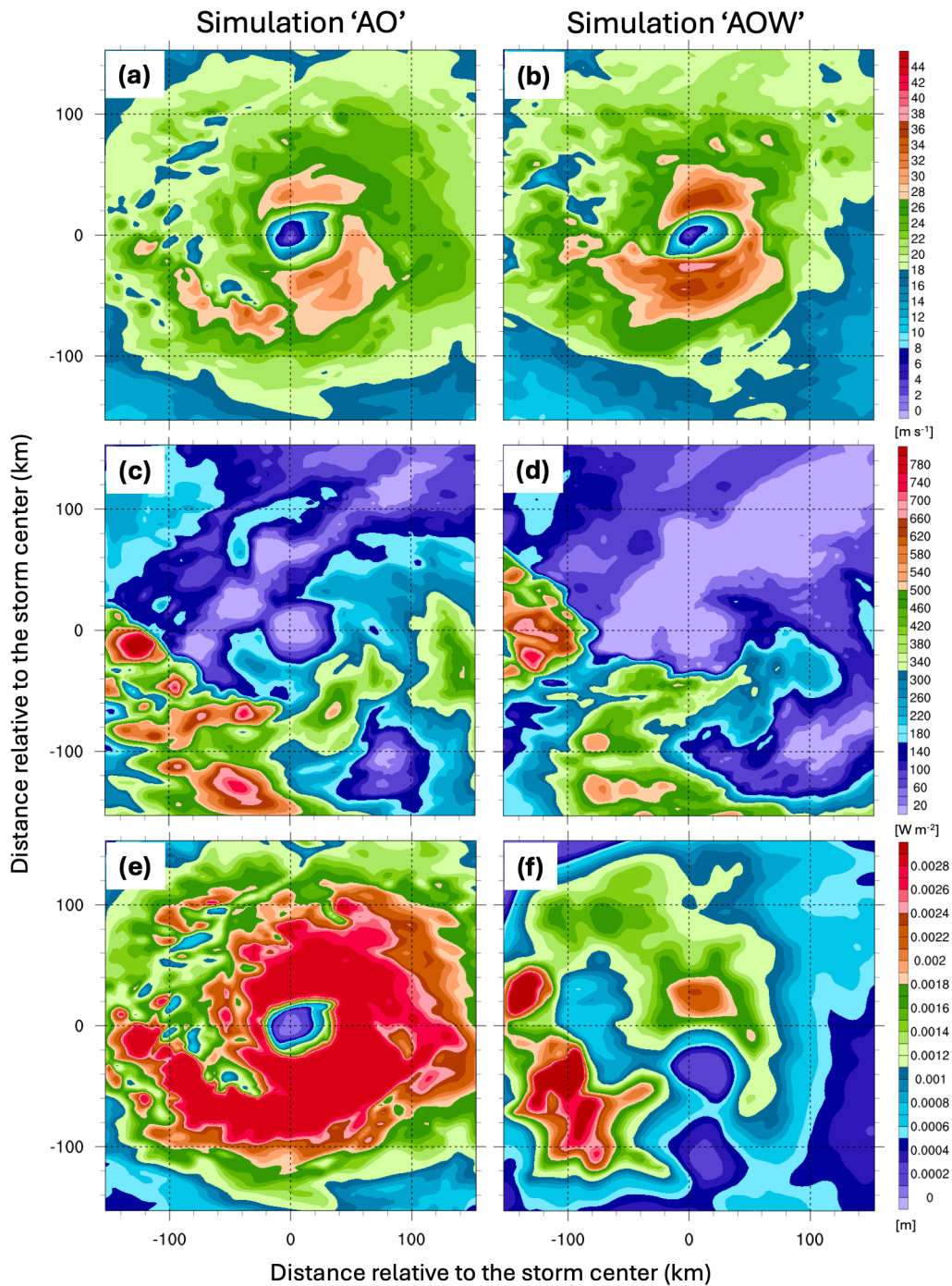
407 **5 Mechanisms Underlying the Improvement in the Fully Coupled Experiment**

408 Compared to experiments ‘A’ and ‘AO’, ‘AOW’ reduces the overestimation of storm intensity (minimum SLP; Fig. 3) and
 409 improves the storm-scale wind structure (Fig. 4), PDF distribution (Fig. 5), and profiles (Fig. 6) from the near surface to the
 410 upper troposphere. To understand these improvements, we analyze SST and surface enthalpy fluxes in ‘AOW’ versus ‘AO’

411 to assess the role of wave-induced processes in Henri's evolution. Experiment 'A' is excluded since it is atmosphere-only
412 and lacks atmosphere–ocean interactions.

413 Because 'AO' and 'AOW' have very similar storm tracks and translation speeds, we can isolate surface processes—SST,
414 enthalpy flux, and surface roughness length (Z_0)—to evaluate their impact on storm intensity and evolution. In 'AOW', ocean
415 surface waves affect Z_0 , which regulates momentum, heat, and moisture exchange at the air–sea interface. In uncoupled
416 simulations like 'AO', Z_0 ~~follows depends solely on wind speed (e.g., via Charnock's formulation and depends only on wind~~
417 ~~speed, with no explicit dependence on wave-state properties where Z_0 is solely relying on the surface wind speed), ignoring~~
418 ~~wave effects~~. This limits capturing dynamic air–sea interactions during TCs, where sea state significantly influences
419 momentum transfer and storm development. Focusing on 12 UTC, 22 August—about 12 hours before landfall when both
420 simulations reach peak minimum SLP—reveals notable differences in Z_0 distribution (Fig. 11). In 'AO', the distribution and
421 strength of Z_0 closely follow the surface wind speed through the Charnock relation. In contrast, 'AOW' simulation shows a
422 different Z_0 pattern (e.g., Taylor and Yelland, 2001; Drennan et al., 2005; Shimura et al., 2017), with reduced values driven
423 by wave dynamics, highlighting the significant role of waves in modulating air–sea momentum and energy exchange (Figs.
424 11a–b, e–f). Prior studies have shown that drag coefficient (C_d) saturates or even decreases once wind speeds exceed
425 approximately 30–35 m s⁻¹, largely due to wave processes which dampen momentum transfer to the ocean (e.g., Donelan et
426 al., 2004; Powell et al., 2003). Since surface roughness length (Z_0) is directly correlated with C_d via Monin-Obukhov theory,
427 this saturation implies a corresponding weakening or plateauing of surface roughness.

428 The influence of ocean surface waves extends beyond modifying Z_0 . Although 'AOW' exhibits stronger winds, it also shows
429 lower SST and reduced surface enthalpy flux compared to 'AO' (Figs. 7l,p, and 11c-d). The primary driver of SST cooling
430 under TCs is ocean vertical mixing. Storm-induced surface winds generate frictional stress, which drives upper-ocean currents
431 and promotes evaporation. Vertical shear in these currents produces turbulence that mixes cooler subsurface water into the
432 mixed layer, reducing SST (e.g., Zhou et al., 2023). This process occurs in both 'AO' and 'AOW'. However, 'AOW'
433 introduces additional vertical mixing through wave dynamics. As surface winds generate waves, momentum is transferred
434 into the ocean. Breaking waves inject momentum deeper, enhancing shear and mixing. Long period, large wave height non-
435 breaking waves that are generated by TCs further deepen the vertical mixing, amplifying SST cooling. These wave-induced
436 processes in 'AOW' lead to cooler SSTs and lower enthalpy fluxes than in 'AO' (Fig. 11). Additionally, the reduced Z_0 in
437 'AOW' corresponds to a lower C_d resulting in less surface roughness and higher near-surface wind speeds due to the inclusion
438 of wave effects.



439

440

441

442

Figure 11. Distribution of (a)-(b) 10-m wind speed (m s^{-1}), (c)-(d) surface enthalpy flux (W m^{-2}), and (e)-(f) surface roughness length (m) derived from the experiment 'AO' (left column) and the experiment 'AOW' (right column) at 12 UTC on 22 August 2021. All distributions are displayed in a $300 \text{ km} \times 300 \text{ km}$ storm-centered coordinate.

443 An important question remains regarding the discrepancy between minimum SLP and maximum wind speed in ‘AO’ and
 444 ‘AOW’ simulations. Although ‘AO’ produces a lower minimum SLP, it shows weaker maximum wind speeds than ‘AOW’—
 445 despite higher surface enthalpy and momentum fluxes at peak intensity (12 UTC, 22 August; Figs. 3b–c, 11a–b). As discussed,
 446 this is due in part to the higher Z_0 in ‘AO’, resulting from the absence of wave dynamics. Increased Z_0 leads to greater
 447 frictional drag, reducing near-surface wind speeds. This enhanced friction contributes to stronger subgradient winds, where
 448 actual wind speeds fall below those expected from gradient wind balance. The imbalance between forces in the boundary
 449 layer is described by the agradiant force (AF), defined as:

$$450$$

$$451 \quad \text{Agradiant Force (AF)} = -\frac{1}{\rho} \frac{\partial p}{\partial r} + \frac{V_t^2}{r} + fV_t \quad (3)$$

$$452$$

453 where p is pressure, r is the radial distance from the TC center, V_t is the tangential wind speed, ρ is air density, and f is the
 454 Coriolis parameter. Near the surface, both ‘AO’ and ‘AOW’ deviate from gradient wind balance due to friction, which reduces
 455 V_t , weakening both the Coriolis and centrifugal forces. With the pressure gradient force unchanged, this creates a negative
 456 agradiant force ($AF < 0$), driving radial inflow. This inflow forms part of the storm’s secondary circulation. Its strength can
 457 indicate the degree of deviation from gradient wind balance—stronger inflow implies greater subgradient winds. Table 4
 458 clearly shows that ‘AO’ is associated with a stronger surface pressure gradient force, which, along with a higher Z_0 , creates
 459 more favorable conditions for enhanced mass flux inflow. On the other hand, ‘AO’ exhibits weaker absolute angular
 460 momentum (AAM), defined as:

$$461$$

$$462 \quad M = rV_t + \frac{1}{2}fr^2 \quad (4)$$

$$463$$

464 As shown in Equation 4, AAM is closely tied to the storm’s rotational wind structure. Therefore, to better understand the
 465 discrepancy between ‘AO’ and ‘AOW’—specifically why ‘AO’ has a stronger pressure gradient but weaker winds—we
 466 analyze the AAM budget, following Zhang and Marks (2015) and Zhao et al. (2022). The AAM budget equation used is:

$$467$$

$$468 \quad \frac{\partial \langle M \rangle}{\partial t} = -\langle V_r \rangle \frac{\partial \langle M \rangle}{\partial r} - \langle w \rangle \frac{\partial \langle M \rangle}{\partial z} - \langle V_r' \rangle \frac{\partial M'}{\partial r} - \langle w' \rangle \frac{\partial M'}{\partial z} + F_r \quad (5)$$

$$469$$

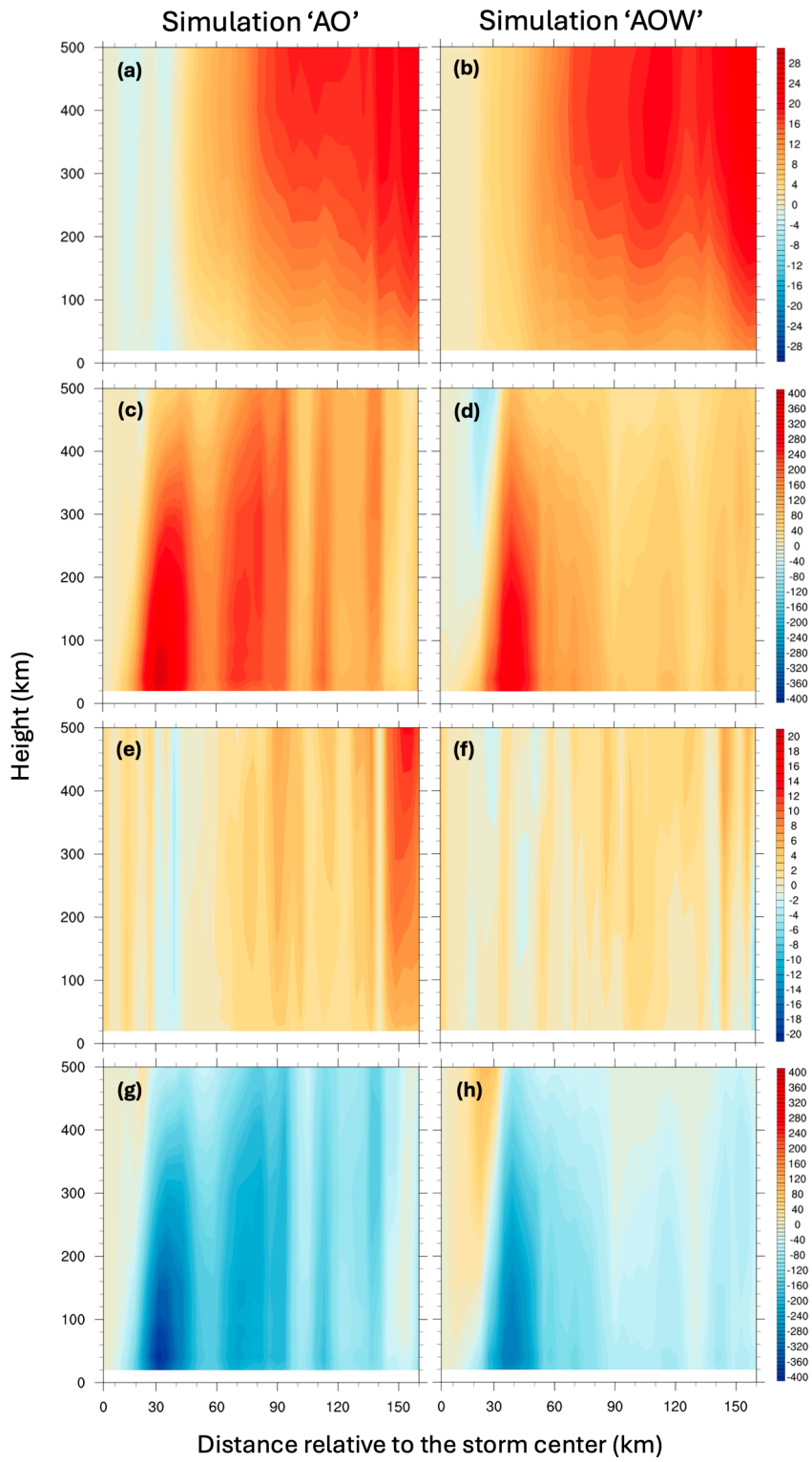
470 where V_r and w denote radial wind speed and vertical wind component, respectively. Brackets $\langle \rangle$ denote azimuthal averages,
 471 and primes indicate deviations from the mean. The left-hand side represents the time tendency of azimuthally averaged AAM.
 472 The right-hand side includes contributions from mean radial advection, mean vertical advection, radial eddy transport, vertical
 473 eddy transport, and friction/residual term F_r . We hypothesize that the higher Z_0 in ‘AO’—a result of the simplified Charnock
 474 relation—enhances angular momentum dissipation and reduces wind speeds despite a stronger pressure gradient. Figure 12

475 presents the AAM tendency, mean radial advection, mean radial eddy transport, and F_r terms over the period from 00 UTC
 476 to 12 UTC on 22 August 2021, during which both storms underwent steady intensification. The results indicate that the mean
 477 radial advection (Figure 12b, f) and F_r (Figure 12d, h) terms are particularly influential in determining the AAM tendency
 478 and tend to oppose each other. Within 100 km of the storm center, substantial AAM dissipation is observed in the F_r term for
 479 both simulations (Figure 12d, h), aligning spatially with regions of elevated Z_0 . However, this dissipation is much more
 480 pronounced in ‘AO’ (Figure 12d), suggesting that its higher Z_0 values may unrealistically amplify angular momentum loss,
 481 leading to weaker surface winds despite lower minimum SLP. These findings highlight the crucial role of air-sea interactions,
 482 particularly those induced by waves and related processes, in accurately simulating the wind structure of TCs within the
 483 marine boundary layer which impact offshore wind turbines.

484
 485 **Table 4. Spatially averaged metrics within 10–60 km of the storm center, vertically integrated through the boundary layer up to**
 486 **1.2 km above the ground level, at 12 UTC on 22 August 2021. PGF indicates pressure gradient force and is calculated at mean sea**
 487 **level.**

Experiment	BL inflow mass flux (kg m^{-3})	BL vertical mass flux (kg m^{-3})	BL AAM ($\text{m}^2 \text{s}^{-1}$)	PGF (m s^{-2})
AO	1.93×10^4	1.34×10^3	1.55×10^{10}	-1.52×10^2
AOW	1.80×10^4	1.33×10^3	1.61×10^{10}	-1.46×10^2

488
 489



491 **Figure 12. Radius-height plots of the terms in the azimuthally averaged absolute angular momentum budget: The radius-height**
492 **plots of the terms in azimuthally averaged absolute angular momentum budget (a)-(b) time tendency term ($\text{m}^2 \text{s}^{-2}$), (b) mean**
493 **advection term ($\text{m}^2 \text{s}^{-2}$), (c) eddy transport term ($\text{m}^2 \text{s}^{-2}$), and (d) friction ($\text{m}^2 \text{s}^{-2}$) and residual term in ‘AO’ during the time from**
494 **00 UTC to 12 UTC 22 August 2021. The bottom-left column is derived from ‘AO’ and the right column from ‘AOW.’ panels (e)-(h)**
495 **are the same as the top panels but for ‘AOW.’**

496 6 Summary and Discussion

497 Previous studies of TC wind fields and their impacts on offshore wind turbines have primarily relied on atmosphere-only or
498 empirical models, which neglect critical interactions among the atmosphere, ocean, and waves. This limitation hampers the
499 accuracy of risk assessments for offshore wind infrastructure, particularly in hurricane-prone regions. This study developed
500 a fully coupled modeling system (C-WFS) integrating WRF, FVCOM, and SWAN to simulate atmosphere-ocean-wave
501 feedback on TC development and assess implications for offshore infrastructure. Using Hurricane Henri (2021) as a case
502 study, chosen for its impact on the U.S. Northeast and available airborne observations, we ran three experiments of increasing
503 complexity: ‘A’, ‘AO’, and ‘AOW.’ These were evaluated against observations. All simulations overestimated intensity in
504 terms of minimum SLP, but the fully coupled ‘AOW’ reduced this bias during development and weakening stages. ‘AOW’
505 also better captured 3D storm structure, especially low-level winds critical to coastal and offshore energy infrastructure. This
506 improvement is attributed to wave-induced ocean mixing (cooling SST) and reduced surface roughness, resulting in more
507 realistic wind fields and lower frictional loss of angular momentum. In contrast, ‘AO’, which lacks wave coupling, exhibited
508 excessive surface roughness from simplified wind only dependent parameterization, causing greater frictional dissipation and
509 weaker tangential winds despite a deeper central pressure. These results highlight the importance of including wave dynamics
510 and incorporating dynamic and thermodynamic feedback among all three components for accurate TC intensity and structural
511 forecasts.

512 The model also captures wind-wave misalignment and alignment, key processes often overlooked but crucial for evaluating
513 structural loads, fatigue, and operational risks. Together, these enhancements yield a more realistic representation of storm
514 evolution, intensity, and structure, underscoring the importance of fully coupled modeling systems for accurate risk
515 assessments and the development of resilient offshore wind infrastructure.

516 While this study applied C-WFS framework to Category 1 Hurricane Henri and highlighted the role of air-sea interactions in
517 TC structure and intensity, it has not yet been applied to stronger storms or included sea spray effects, both of which are
518 current limitations we are actively addressing. A key motivation behind this work is to better understand how coupled
519 dynamics modulate TC wind fields across different intensities, particularly in regions with offshore wind farms, where storm
520 structure and intensity can directly affect turbine loading, resilience, and operational risk.

521 Another open question is how the horizontal resolution of ocean components influences TC development in coupled models.
522 While it is well established that finer atmospheric resolution improves storm intensity forecasts (e.g., Gentry and Lakmann,
523 2010; Prein et al., 2015), the effects of ocean resolution are less understood. Higher-resolution ocean grids can better resolve
524 mesoscale and submesoscale features such as eddies and fronts, which influence SST patterns, air-sea fluxes, and upper-
525 ocean mixing—factors critical to storm intensity and evolution (Zhang et al., 2023). These processes modulate SST cooling

526 and ocean heat content redistribution during storm passage. Unlike traditional nested-grid approaches (e.g., in COAWST),
527 C-WFS uses an unstructured mesh that smoothly transitions across resolutions, avoiding boundary artifacts. This flexibility
528 makes C-WFS particularly well suited to explore how ocean resolution affects coupled dynamics and TC behavior—an area
529 we aim to investigate in future work.

530 In parallel, this modeling framework presents a valuable opportunity to assess whether current IEC (2019a, 2019b) standards
531 for wind conditions, such as wind shear, veer, and turbulence are adequate for regions prone to TCs. We are currently
532 performing a comprehensive analysis using this fully coupled model to characterize the representation of these wind
533 parameters, potentially informing revisions to design criteria that improve the structural resilience and reliability of offshore
534 wind turbines under TC-induced loading conditions.

535

536 **Code and data availability.** The WRF model (Version 4.5.1) is described by Skamarock et al. (2019), and its code is publicly
537 available from <https://github.com/wrf-model/WRF> (University Corporation for Atmospheric Research, 2019). The code for
538 FVCOM (Version 4.3.1., Chen et al., 2003, 2013) for ocean circulation model is publicly available at
539 <https://github.com/FVCOM-GitHub/fvcom>. The SWAN (Version 41.01, Booij et al., 1999) is a third-generation spectral
540 wave model developed at Delft University of Technology that computes random, short-crested wind-generated waves in
541 coastal regions and inland waters (<http://swanmodel.sourceforge.net/>). HYbrid Coordinate Ocean Model (HYCOM;
542 Cummings and Smedstad, 2014) analysis data used for ocean model forcing is available at <http://hycom.org/dataserver/>.
543 NCEP provides Global Forecast System (GFS; NCEP, 2015) data, which is used as atmospheric forcing data, available at
544 <https://www.nco.ncep.noaa.gov/pmb/products/gfs/>. The OSTIA (Good et al., 2020) global sea surface temperature provides
545 daily maps of foundation sea surface temperature at $0.05^\circ \times 0.05^\circ$ available from
546 https://data.marine.copernicus.eu/product/SST_GLO_SST_L4_REP_OBSERVATIONS_010_011/description. The NCL
547 and Python codes for performing analysis and visualization are available at <https://www.ncl.ucar.edu/> and
548 <https://www.python.org/downloads/>, respectively. All simulation data are available from the authors upon request.

549

550 **Author contribution.** Conceptualization, Formal analysis, Validation, Visualization: CJ, JW, PX, CH, WP; Data curation,
551 Investigation, Software: CJ, JW, CH, MB, GN; Funding acquisition, Resources, Supervision: JW, PX, WP; Methodology:
552 CJ, CH, WP; Project administration: JW, PX; Writing – original draft: CJ, JW, PX, WP; Writing – review & editing: CJ, JW,
553 PX, CH, MB, GN.

554 **Competing interests.** The authors declare that they have no competing interests.

555 **Acknowledgements.** This study is supported by the Wind Energy Technologies Office (WETO) of the U.S. Department of
556 Energy (DOE) Office of Energy Efficiency and Renewable Energy. The WRF model was made available by the National
557 Center for Atmospheric Research, which is sponsored by NSF. High-Performance Computing support from the Theta cluster
558 operated by Argonne Leadership Computing Facility (ALCF) and Kestrel operated by National Renewable Energy
559 Laboratory (NREL).

- 561 Aijaz, S., Ghantous, M., Babanin, A. V., Ginis, I., Thomas, B., and Wake, G.: Nonbreaking wave-induced mixing in upper
562 ocean during tropical cyclones using coupled hurricane-ocean-wave modeling, *Journal of Geophysical Research: Oceans*,
563 122, 3939–3963, <https://doi.org/10.1002/2016JC012586>, 2017.
- 564 Akinsanola, A. A., Jung, C., Wang, J., and Kotamarthi, V. R.: Evaluation of precipitation across the contiguous United
565 States, Alaska, and Puerto Rico in multi-decadal convection-permitting simulations, *Scientific Reports*, 14, 1238, 2024.
- 566 Arthur, W. C.: A statistical–parametric model of tropical cyclones for hazard assessment, *Natural Hazards and Earth
567 System Sciences*, 21, 893–916, <https://doi.org/10.5194/nhess-21-893-2021>, 2021.
- 568 Barr, B. W. and Chen, S. S.: Impacts of seastate-dependent sea spray heat fluxes on tropical cyclone structure and intensity
569 in fully coupled atmosphere-wave-ocean model simulations, *Journal of Advances in Modeling Earth Systems*, 17,
570 e2024MS004550. <https://doi.org/10.1029/2024MS004550>, 2024.
- 571 Booij, N., Ris, R. C., and Holthuijsen, L. H.: A third-generation wave model for coastal regions. Part I: Model description
572 and validation, *Journal of Geophysical Research*, 104, 7649–7666, <https://doi.org/10.1029/98JC02622>, 1999.
- 573 Charnock, H., 1955: Wind stress on a water surface. *Quart. J. Roy. Meteor. Soc.*, 81, 639–640.
- 574 Chen, C., Beardsley, R. C., and Cowles, G.: An unstructured grid, finite-volume coastal ocean model: FVCOM user manual,
575 Technical Report SMAST/UMASSD-13-0701, 416 pp., 2013.
- 576 Chen, C., Liu, H., and Beardsley, R. C.: An unstructured grid, finite-volume, three-dimensional, primitive equations ocean
577 model: Application to coastal ocean and estuaries, *Journal of Atmospheric and Oceanic Technology*, 20, 159–186,
578 [https://doi.org/10.1175/1520-0426\(2003\)020<0159:AUGFVT>2.0.CO;2](https://doi.org/10.1175/1520-0426(2003)020<0159:AUGFVT>2.0.CO;2), 2003.
- 579 Chen, P., Zhang, Z., Li, Y., Ye, R., Li, R., and Song, Z.: The two-parameter Holland pressure model for tropical cyclones,
580 *Journal of Marine Science and Engineering*, 12, 92, <https://doi.org/10.3390/jmse12010092>, 2024.
- 581 Chen, S. S., Price, J. F., Zhao, W., Donelan, M. A., and Walsh, E. J.: The CBLAST-hurricane program and the next-
582 generation fully coupled atmosphere–wave–ocean models for hurricane research and prediction, *Bulletin of the
583 American Meteorological Society*, 88, 311–318, 2007.
- 584 Chen, S. S., Zhao, W., Donelan, M. A., and Tolman, H. L.: Directional wind–wave coupling in fully coupled atmosphere–
585 wave–ocean models: Results from CBLAST-Hurricane, *Journal of the Atmospheric Sciences*, 70, 3198–3215, 2013.
- 586 Craig, A., Valcke, S., and Coquart, L.: Development and performance of a new version of the OASIS coupler, OASIS3-
587 MCT_3.0, *Geoscientific Model Development*, 10, 3297–3308, <https://doi.org/10.5194/gmd-10-3297-2017>, 2017.
- 588 Creasey, R. L., and Elsberry, R. L.: Tropical cyclone center positions from sequences of HDSS sondes deployed along
589 high-altitude overpasses. *Wea. Forecasting*, 32, 317–325, <https://doi.org/10.1175/WAF-D-16-0096.1>, 2017.
- 590 Cummings, J. A. and Smedstad, O. M.: Ocean data impacts in global HYCOM, *Journal of Atmospheric and Oceanic
591 Technology*, 31, 1771–1791, <https://doi.org/10.1175/JTECH-D-14-00011.1>, 2014.
- 592 DeMaria, M., Knaff, J. A., and Sampson, C.: Evaluation of long-term trends in tropical cyclone intensity forecasts,
593 *Meteorology and Atmospheric Physics*, 97, 19–28, 2007.
- 594 DeMaria, M., Sampson, C. R., Knaff, J. A., and Musgrave, K. D.: Is tropical cyclone intensity guidance improving?,
595 *Bulletin of the American Meteorological Society*, 95, 387–398, <https://doi.org/10.1175/bams-d-12-00240.1>, 2014.

596 Donelan, M. A. et al. On the limiting aerodynamic roughness of the ocean in very strong winds. *Geophys. Res. Lett.* 31,
597 L18306, 10.1029/2004GL019460, 2004.

598 Drennan, W. M., Graber, H. C., Hauser, D., and Quentin, C.: On the wave age dependence of wind stress over pure wind
599 seas, *Journal of Geophysical Research: Oceans*, 108, 8062, 2003.

600 Drennan, W. M., Taylor, P. K., and Yelland, M. J., “Parameterizing the sea surface roughness,” *J. Phys. Oceanogr.* 35(5),
601 835–848, 2005.

602 Dyer, A. J. and Hicks, B. B.: Flux-gradient relationships in the constant flux layer, *Quarterly Journal of the Royal*
603 *Meteorological Society*, 96, 715–721, 1970.

604 Emanuel, K. A.: An air-sea interaction model of the tropical cyclones. Part I: Steady-State Maintenance, *Journal of the*
605 *Atmospheric Sciences*, 43, 585–605, [https://doi.org/10.1175/1520-0469\(1986\)043<0585:AASITF>2.0.CO;2](https://doi.org/10.1175/1520-0469(1986)043<0585:AASITF>2.0.CO;2), 1986.

606 Fan, Y., Ginis, I., and Hara, T.: The effect of wind–wave–current interaction on air–sea momentum fluxes and ocean
607 response in tropical cyclones, *Journal of Physical Oceanography*, 39, 1019–1034, 2009.

608 Fischer, M. S., Reasor, P. D., Rogers, R. F., and Gamache, J. F.: An analysis of tropical cyclone vortex and convective
609 characteristics in relation to storm intensity using a novel airborne doppler radar database, *Monthly Weather Review*,
610 150, 2255–2278, <https://doi.org/10.1175/MWR-D-21-0223.1>, 2022.

611 Gentry, M. A. and Lackmann, G. M.: Sensitivity of simulated tropical cyclone structure and intensity to horizontal
612 resolution, *Monthly Weather Review*, 138, 688–704, 2010.

613 Ghantous, M. and Babanin, A. V.: One-dimensional modeling of upper ocean mixing by turbulence due to wave orbital
614 motion, *Nonlinear Processes in Geophysics*, 21, 325–338, <https://doi.org/10.5194/npg-21-325-2014>, 2014a.

615 Ghantous, M. and Babanin, A. V.: Ocean mixing by wave orbital motion, *Acta Physica Slovaca*, 64, 1–57,
616 <https://doi.org/10.2478/apsrt-2014-0001>, 2014b.

617 Good, S., Fiedler, E., Mao, C., Martin, M. J., Maycock, A., Reid, R., Roberts-Jones, J., Searle, T., Waters, J., While, J.,
618 and Worsfold, M.: The current configuration of the OSTIA system for operational production of foundation sea surface
619 temperature and ice concentration analyses, *Remote Sensing*, 12, 720, <https://doi.org/10.3390/rs12040720>, 2020.

620 Hong, S.-Y. and Lim, J.-O.: The WRF single-moment 6-class microphysics scheme (WSM6), *Journal of the Korean*
621 *Meteorological Society*, 42, 129–151, 2006.

622 Hong, S.-Y., Noh, Y., and Dudhia, J.: A new vertical diffusion package with an explicit treatment of entrainment processes,
623 *Monthly Weather Review*, 134, 2318–2341, 2006.

624 Iacono, M. J., Delamere, J. S., Mlawer, E. J., Shephard, M. W., Clough, S. A., and Collins, W. D.: Radiative forcing by
625 long-lived greenhouse gases: Calculations with the AER radiative transfer models, *Journal of Geophysical Research*,
626 113, D13103, <https://doi.org/10.1029/2007JD009277>, 2008.

627 IEC: Wind turbines - part 1: Design requirements (No. IEC 61400-1:2019), 2019a.

628 IEC: Wind turbines – part 3: Design requirements for offshore wind turbines (No. IEC 61400-3-1:2019), 2019b

629 Itiki, R., Manjrekar, M., Di Santo, S. G., and Itiki, C.: Method for spatiotemporal wind power generation profile under
630 hurricanes: US-Caribbean super grid proposition, *Renewable and Sustainable Energy Reviews*, 173, 113082, 2023.

631 Jimenez, P., Dudhia, J., Gonzalez-Ruoco, J. F., Navarro, J., Montavez, J. P., and Garcia-Bustamente, E.: A revised scheme
632 for the WRF surface layer formulation, *Monthly Weather Review*, 140, 898–918, 2012.

633 Knapp, K. R., Kruk, M. C., Levinson, D. H., Diamond, H. J., and Neumann, C. J.: The international best track archive for
634 climate stewardship (IBTrACS) unifying tropical cyclone data, *Bulletin of the American Meteorological Society*, 91,
635 363–376, 2010.

636 Komen, G. J., Hasselmann, K., and Hasselmann, S.: On the existence of a fully developed wind-sea spectrum, *Journal of*
637 *Physical Oceanography*, 14, 1271–1285, [https://doi.org/10.1175/1520-0485\(1984\)014<1271:OTEOAF>2.0.CO;2](https://doi.org/10.1175/1520-0485(1984)014<1271:OTEOAF>2.0.CO;2), 1984.

638 Kouadio, K., Bastin, S., Konare, A., and Ajayi, V. O.: Does convection-permitting simulate better rainfall distribution and
639 extreme over Guinean coast and surroundings?, *Climate Dynamics*, 55, 153–174, [https://doi.org/10.1007/s00382-018-](https://doi.org/10.1007/s00382-018-4308-y)
640 4308-y, 2020.

641 Ma, T. and Sun, C.: Large Eddy Simulation of Combined Wind-wave Loading on Offshore Wind Turbines, arXiv [preprint],
642 arXiv:2310.03407, 2023.

643 Madsen, O. S., Poon, Y. K., and Graber, H. C.: Spectral wave attenuation by bottom friction: Theory, in: *Proceedings of*
644 *the International Conference on Coastal Engineering*, 21, 492–506, 1988.

645 Mellor, G. L. and Yamada, T.: Development of a turbulence closure model for geophysical fluid problems, *Reviews of*
646 *Geophysics*, 20, 851–875, <https://doi.org/10.1029/RG020i004p00851>, 1982.

647 Nakanishi, M. and Niino, H.: Development of an improved turbulence closure model for the atmospheric boundary layer,
648 *Journal of the Meteorological Society of Japan*, 87, 895–912, <https://doi.org/10.2151/jmsj.87.895>, 2009.

649 National Data Buoy Center (NDBC), NOAA: National Data Buoy Center (NDBC) Moored Buoy and C-MAN Station Data,
650 UCAR/NCAR - Earth Observing Laboratory, <https://doi.org/10.26023/V640-H29S-MR0S>, 2008.

651 National Centers for Environmental Prediction (NCEP): NCEP GFS 0.25 Degree Global Forecast Grids Historical Archive,
652 Research Data Archive at the National Center for Atmospheric Research, Computational and Information Systems
653 Laboratory, <https://doi.org/10.5065/D65D8PWK>, 2015.

654 Olson, J. B., Kenyon, J. S., Angevine, W. M., Brown, J. M., Pagowski, M., and Sušelj, K.: A description of the MYNN-
655 EDMF scheme and coupling to other components in WRF-ARW, NOAA Technical Memorandum OAR GSD No. 61,
656 37 pp., <https://doi.org/10.25923/n9wm-be49>, 2019.

657 Paulson, C. A.: The mathematical representation of wind speed and temperature profiles in the unstable atmospheric surface
658 layer, *Journal of Applied Meteorology*, 9, 857–861, 1970.

659 Powell, M. D., Vickery, P. J. & Reinhold, T. A. Reduced drag coefficient for high wind speeds in tropical cyclones. *Nature*
660 422, 279–283, 2003.

661 Prein, A. F., Langhans, W., Fosser, G., Ferrone, A., Ban, N., Goergen, K., Keller, M., Tölle, M., Gutjahr, O., Feser, F., et
662 al.: A review on regional convection-permitting climate modeling: Demonstrations, prospects, and challenges, *Reviews*
663 *of Geophysics*, 53, 323–361, <https://doi.org/10.1002/2014RG000475>, 2015.

664 Pringle, W. J. and Kotamarthi, V. R.: Coupled ocean wave-atmosphere models for offshore wind energy, Argonne National
665 Laboratory, <https://doi.org/10.2172/1829093>, 2021.

666 Qing, Y. and Wang, S.: Multi-decadal convection-permitting climate projections for China’s Greater Bay Area and
667 surroundings, *Climate Dynamics*, <https://doi.org/10.1007/s00382-021-05716-w>, 2021.

668 Rappaport, E. N., et al.: Advances and challenges at the National Hurricane Center, *Weather and Forecasting*, 24, 395–419,
669 2009.

670 Roldán, M., Montoya, R. D., Rios, J. D., and Osorio, A. F.: Modified parametric hurricane wind model to improve the
671 asymmetry in the region of maximum winds, *Ocean Engineering*, 280, 114508,
672 <https://doi.org/10.1016/j.oceaneng.2023.114508>, 2023.

673 Sanchez Gomez, M., Lundquist, J. K., Mirocha, J. D., and Arthur, R. S.: Investigating the physical mechanisms that modify
674 wind plant blockage in stable boundary layers, *Wind Energy Science*, 8, 1049–1069, [https://doi.org/10.5194/wes-8-1049-](https://doi.org/10.5194/wes-8-1049-2023)
675 [2023](https://doi.org/10.5194/wes-8-1049-2023), 2023.

676 Schade, L. R. and Emanuel, K. A.: The ocean's effect on the intensity of tropical cyclones: Results from a simple coupled
677 atmosphere–ocean model, *Journal of the Atmospheric Sciences*, 56, 642–651, 1999.

678 Shanahan, T. and Fitzgerald, B.: Wind–Wave Misalignment in Irish Waters and Its Impact on Floating Offshore Wind
679 Turbines. *Energies*, 18(2), 372; <https://doi.org/10.3390/en18020372>, 2025.

680 Shimura, T., Noh, Y., and Hara, T.: Long-term impacts of ocean wave-dependent roughness on global climate systems, *J.*
681 *Geophys. Research: Oceans*, 122(3), 1995–2011, <https://doi.org/10.1002/2016JC012621>, 2017.

682 Skamarock, W. C., Klemp, J. B., Dudhia, J., Gill, D. O., Liu, Z., Berner, J., Wang, W., Powers, J. G., Duda, M. G., and
683 Barker, D. M.: A description of the advanced research WRF model version 4, 145 pp., National Center for Atmospheric
684 Research, 2019.

685 Smagorinsky, J.: General circulation experiments with the primitive equations, part I: the basic experiment, *Monthly*
686 *Weather Review*, 91, 99–164, 1963.

687 Smith, A. B.: 2010–2019: A landmark decade of U.S. billion-dollar weather and climate disasters, NOAA,
688 [https://www.climate.gov/news-features/blogs/beyond-data/2010-2019-landmark-decade-us-billion-dollar-weather-and-](https://www.climate.gov/news-features/blogs/beyond-data/2010-2019-landmark-decade-us-billion-dollar-weather-and-climate)
689 [climate](https://www.climate.gov/news-features/blogs/beyond-data/2010-2019-landmark-decade-us-billion-dollar-weather-and-climate), 2020.

690 Sun, X., Xue, M., Brotzge, J., McPherson, R. A., Hu, X.-M., and Yang, X.-Q.: An evaluation of dynamical downscaling
691 of Central Plains summer precipitation using a WRF-based regional climate model at a convection-permitting 4 km
692 resolution, *Journal of Geophysical Research: Atmospheres*, 121, 13801–13825, <https://doi.org/10.1002/2016JD024796>,
693 2016.

694 Taylor, P. K. and Yelland, M. J.: The dependence of sea surface roughness on the height and steepness of the waves,
695 *Journal of Physical Oceanography*, 31, 572–590, 2001.

696 Wada, A. and Usui, N.: Impacts of oceanic preexisting conditions on predictions of Typhoon Hai-Tang in 2005, *Advances*
697 *in Meteorology*, 2010, 756071, 2010.

698 Warner, J. C., Armstrong, B., He, R., and Zambon, J. B.: Development of a coupled ocean–atmosphere–wave–sediment
699 transport (COAWST) modeling system, *Ocean Modelling*, 35, 230–244,
700 <https://doi.org/10.1016/j.oceanmod.2010.07.010>, 2010.

701 Webb, E. K.: Profile relationships: The log-linear range, and extension to strong stability, *Quarterly Journal of the Royal*
702 *Meteorological Society*, 96, 67–90, 1970.

703 Wei, J., Jiang, G. Q., and Liu, X.: Parameterization of typhoon-induced ocean cooling using temperature equation and
704 machine learning algorithms: An example of Typhoon Soulik (2013), *Ocean Dynamics*, 67, 1179–1193,
705 <https://doi.org/10.1007/s10236-017-1082-z>, 2017.

706 Wright, C. W., et al.: Hurricane directional wave spectrum spatial variation in the open ocean, *Journal of Physical*
707 *Oceanography*, 31, 2472–2488, 2001.

708 Wu, L., Rutgersson, A., Sahlée, E., and Guo Larsén, X.: Swell impact on wind stress and atmospheric mixing in a regional
709 coupled atmosphere-wave model, *Journal of Geophysical Research: Oceans*, 121, 4633–4648,
710 <https://doi.org/10.1002/2015JC011576>, 2016.

711 Xu, X., Voermans, J. J., Zhang, W., Zhao, B., Qiao, F., Liu, Q., Moon, I.-J., Janekovic, I., Waseda, T., and Babanin, A. V.:
712 Tropical cyclone modeling with the inclusion of wave-coupled processes: sea spray and wave turbulence, *Geophys. Res.*
713 *Lett.*, 50, e2023GL106536, <https://doi.org/10.1029/2023GL106536>, 2023.

714 Yamaguchi, M., Ishida, J., Sato, H., and Nakagawa, M.: WGNE intercomparison of tropical cyclone forecasts by
715 operational nwp models: A quarter century and beyond, *Bulletin of the American Meteorological Society*, 98, 2337–
716 2349, <https://doi.org/10.1175/bams-d-16-0133.1>, 2017.

717 Zambon, J. B., He, R., and Warner, J. C.: Investigation of Hurricane Ivan using the coupled ocean–atmosphere–wave–
718 sediment transport (COAWST) model, *Ocean Dynamics*, 64, 1535–1554, <https://doi.org/10.1007/s10236-014-0777-7>,
719 2014.

720 Zambon, J. B., He, R., Warner, J. C., and Hegermiller, C. A.: Impact of SST and surface waves on Hurricane Florence
721 (2018): A coupled modeling investigation, *Weather and Forecasting*, 36, 1713–1734, <https://doi.org/10.1175/WAF-D-20-0171.1>, 2021.

722

723 Zhang, J. A. and Marks, F. D.: Effects of horizontal diffusion on tropical cyclone intensity change and Xd structure in
724 idealized three-dimensional numerical simulations, *Monthly Weather Review*, 143, 3981–3995,
725 <https://doi.org/10.1175/mwr-d-14-00341.1>, 2015.

726 Zhang, S., Xu, S., Fu, H., Wu, L., Liu, Z., Gao, Y., et al.: Toward earth system modeling with resolved clouds and ocean
727 submesoscales on heterogeneous many-core HPCs, *National Science Review*, 10, nwad069, 2023.

728 Zhao, B., Qiao, F., Cavaleri, L., Wang, G., Bertotti, L., and Liu, L.: Sensitivity of typhoon modeling to surface waves and
729 rainfall, *Journal of Geophysical Research: Oceans*, 122, 1702–1723, <https://doi.org/10.1002/2016JC012262>, 2017.

730 Zhao, B., Wang, G., Zhang, J. A., Liu, L., Liu, J., Xu, J., et al.: The effects of ocean surface waves on tropical cyclone
731 intensity: Numerical simulations using a regional atmosphere-ocean-wave coupled model, *Journal of Geophysical*
732 *Research: Oceans*, 127, e2022JC019015, <https://doi.org/10.1029/2022JC019015>, 2022.

733 Zhou, X., Hara, T., Ginis, I., D’Asaro, E., and Reichl, B. G.: Evidence of Langmuir mixing effects in the upper ocean layer
734 during tropical cyclones using observations and a coupled wave-ocean model, *Journal of Geophysical Research: Oceans*,
735 128, e2023JC020062, <https://doi.org/10.1029/2023JC020062>, 2023.